



Chinese Pharmaceutical Association
Institute of Materia Medica, Chinese Academy of Medical Sciences

Acta Pharmaceutica Sinica B

www.elsevier.com/locate/apsb
www.sciencedirect.com



ORIGINAL ARTICLE

Inhalable metal–organic framework-mediated cuproptosis combined with PD-L1 checkpoint blockade for lung metastasis synergistic immunotherapy



Chongzheng Yan^{a,b}, Ying Liu^{a,b}, Guozhi Zhao^{a,b}, Huatian Yang^{a,b},
Huaiyou Lv^{a,b}, Genju Li^{a,b}, Yuhan Li^{a,b}, Yaqing Fu^{a,b}, Fengqin Sun^{a,b},
Yafei Feng^{a,b}, Yizhe Li^{a,b}, Zhongxi Zhao^{a,b,*}

^aDepartment of Pharmaceutics, Key Laboratory of Chemical Biology of Ministry of Education, School of Pharmaceutical Sciences, Cheelloo College of Medicine, Shandong University, Jinan 250012, China

^bKey University Laboratory of Pharmaceutics & Drug Delivery Systems of Shandong Province, School of Pharmaceutical Sciences, Cheelloo College of Medicine, Shandong University, Jinan 250012, China

Received 18 September 2023; received in revised form 5 December 2023; accepted 15 December 2023

KEY WORDS

Cuproptosis;
Immunogenic cell death;
PD-L1 checkpoint blockade;
Copper-based metal-organic framework;
Immunotherapy;
Tumor microenvironment;
Transmucosal delivery;
Lung metastasis

Abstract Cuproptosis shows enormous application prospects in lung metastasis treatment. However, the glycolysis, Cu⁺ efflux mechanisms, and insufficient lung drug accumulation severely restrict cuproptosis efficacy. Herein, an inhalable poly (2-(*N*-oxide-*N,N*-diethylamino)ethyl methacrylate) (OPDEA)-coated copper-based metal–organic framework encapsulating pyruvate dehydrogenase kinase 1 siRNA (siPDK) is constructed for mediating cuproptosis and subsequently promoting lung metastasis immunotherapy, namely OMP. After inhalation, OMP shows highly efficient lung accumulation and long-term retention, ascribing to the OPDEA-mediated pulmonary mucosa penetration. Within tumor cells, OMP is degraded to release Cu²⁺ under acidic condition, which will be reduced to toxic Cu⁺ to induce cuproptosis under glutathione (GSH) regulation. Meanwhile, siPDK released from OMP inhibits intracellular glycolysis and adenosine-5'-triphosphate (ATP) production, then blocking the Cu⁺ efflux protein ATP7B, thereby rendering tumor cells more sensitive to OMP-mediated cuproptosis. Moreover, OMP-mediated cuproptosis triggers immunogenic cell death (ICD) to promote dendritic cells (DCs) maturation and CD8⁺ T cells infiltration. Notably, OMP-induced cuproptosis up-regulates membrane-associated programmed cell death-ligand 1 (PD-L1) expression and induces soluble PD-L1 secretion, and thus synergizes with anti-PD-L1 antibodies (aPD-L1) to reprogram immunosuppressive tumor microenvironment, finally yielding

*Corresponding author.

E-mail address: zxzhao@sdu.edu.cn (Zhongxi Zhao).

Peer review under the responsibility of Chinese Pharmaceutical Association and Institute of Materia Medica, Chinese Academy of Medical Sciences.

<https://doi.org/10.1016/j.apsb.2024.01.017>

2211-3835 © 2024 The Authors. Published by Elsevier B.V. on behalf of Chinese Pharmaceutical Association and Institute of Materia Medica, Chinese Academy of Medical Sciences. This is an open access article under the CC BY-NC-ND license (<http://creativecommons.org/licenses/by-nc-nd/4.0/>).

improved immunotherapy efficacy. Overall, OMP may serve as an efficient inhalable nanoplatform and afford preferable efficacy against lung metastasis through inducing cuproptosis and combining with aPD-L1.

© 2024 The Authors. Published by Elsevier B.V. on behalf of Chinese Pharmaceutical Association and Institute of Materia Medica, Chinese Academy of Medical Sciences. This is an open access article under the CC BY-NC-ND license (<http://creativecommons.org/licenses/by-nc-nd/4.0/>).

1. Introduction

Lung metastasis is the spread of tumor cells from other primary tumors to the lungs, which is critical cause of cancer mortality in patients^{1,2}. Currently, the treatment options on hand are surgery, chemotherapy, and radiation therapy^{3,4}. However, these therapies available for lung metastasis are failing because they are only effective in the preliminary stages of the disease and their effects on the survival of patients are still far from satisfactory⁵. Moreover, chemotherapy and radiation therapy are prone to resistance due to the apoptotic mechanism⁶. Immunotherapeutic strategies have shown encouraging results against various cancers. Among the numerous immunotherapeutic strategies available, immune checkpoint blockade (ICB) therapy, such as anti-programmed cell death protein ligand-1 antibodies (aPD-L1), has been effective against lung metastasis, owing to the effect on the restoration of exhausted T cells. However, the responsiveness to immunotherapy among patients is limited. On the one hand, the tumor-associated macrophages (TAMs), regulatory T cells (Tregs), and myeloid-derived suppressor cells (MDSCs) at the lung metastatic sites create a robust suppressive immune microenvironment that significantly promotes cancer cell immune escape^{7,8}. On the other hand, insufficient PD-L1 expression in lung metastasis sites restricts the clinical implementation of aPD-L1⁹. Therefore, it is crucial to develop a synergistic treatment strategy to induce tumor cells death and reverse the immunosuppressive tumor microenvironment (TME) to facilitate effective anti-metastatic therapy.

Very recently, Cu⁺ overload-induced cell death pathway, cuproptosis, was recognized by Tsvetkov et al.,¹⁰ which opens a new horizon for the development of Cu⁺ in cancer treatment. Cuproptosis is distinct from other known cell death pathways, including apoptosis, ferroptosis, pyroptosis, and necroptosis, which is a Cu⁺-dependent cell death pathway characterized by an accumulation of lipid peroxides, and cannot be inhibited by the inhibitors of the above cell death methods. On the one hand, lipoyl synthase (LIAS) and ferredoxin1 (FDX1) factors regulate dihydroipoamide S-acetyltransferase (DLAT) to undergo lipoylation, and Cu⁺ directly binds to lipoylated components of the tricarboxylic acid (TCA) cycle (lipoylated DLAT (Lip-DLAT)), aggregates lipoylated proteins. On the other hand, Cu⁺ destabilizes iron-sulfur (Fe-S) cluster proteins. These two together will lead to proteotoxic stress and eventually induce cell death, namely, cuproptosis. Although promising, glycolysis-dominated metabolism patterns (cells that are more reliant on mitochondrial respiration are nearly 1000-fold more sensitive to Cu⁺ than cells undergoing glycolysis) and Cu⁺-transporting ATP7B (a main Cu⁺ exporter that relies on ATP for energy) in cancer cells inhibit the occurrence of cuproptosis^{10,11}. Therefore, it is a formidable challenge to overcome these hurdles for the enhancement of cuproptosis. Pyruvate dehydrogenase complex (PDH) and

pyruvate dehydrogenase kinase 1 (PDK1) are key mitochondrial enzymes, which could dominate the critical switch between the mitochondrial respiration and glycolysis¹². PDK1 overexpresses in cancer cells and controls the activity of PDH: stimulation in PDK1 could suppress PDH, accordingly restrain pyruvate from entering into mitochondrion, aggravate the glycolysis and increase ATP generation¹³. PDK1 thus represents a promising target in sensitizing tumor cells to cuproptosis. While no therapy is currently clinically available, several PDK1 inhibitors are in the pre-clinical or clinical development stage^{14,15}. RNA interference (RNAi) with small interfering RNA (siRNA) can be used to target any genes of interest with high efficiency and specificity¹⁶. Consequently, suppressing glycolysis and subsequently reducing ATP production by siRNA targeting PDK1 (siPDK) can produce a strong anti-tumor effect *via* cuproptosis. At the same time, cuproptosis can evoke immunogenic cell death (ICD) to release damage-associated molecular patterns (DAMPs), including calreticulin (CRT), high mobility group box 1 (HMGB1), and ATP from dying tumor cells^{17–19}. The release of these “eat me” signals can improve DCs maturation, resulting in the activation of CD8⁺ T cells and the initiation of antitumor immune responses^{20,21}. Moreover, cuproptosis regulates PD-L1 expression, which can reverse immunosuppression tumor microenvironment and enhance the effect of immunotherapy. These findings would be of great significance for the development of the link between cuproptosis and immunotherapy.

Metal-organic frameworks (MOF), composed of organic ligands and metal ions/ion clusters, are considered to be a promising class of siRNA delivery carriers due to the biocompatibility, protecting siRNA from enzyme degradation, and achieving efficient delivery to the site of action^{22,23}. Coincidentally, MOFs can respond to the tumor microenvironment and burst out abundant metal ions. Inspired by this, a nanoplatform was established by encapsulating siPDK into copper-based MOF (MP), which would release Cu²⁺ and siPDK in the acidic microenvironment. In addition, for the improvement of the lung metastasis therapeutic effect, the accurate delivery of MP to the lung lesions is crucially important. A pulmonary inhalation delivery system exhibits many unique advantages such as excellent lung targeting capacity, high drug concentrations in the lung lesions, and low systemic adverse effects, which can be employed as a prospective drug delivery route for lung metastasis treatment^{24–27}. However, the design of inhalable nanomedicines is much more challenging because of the existence of alveolar mucosal barriers^{28,29}. Interestingly, a water-soluble polyzwitterion, poly (2-(*N*-oxide-*N,N*-diethylamino)ethyl methacrylate) (OPDEA) exhibited efficient intestinal mucosal penetration in oral drug delivery³⁰. In light of these findings, the administration of MP with OPDEA cloak may be an ideal candidate to achieve efficient mucosa penetration and lung retention after inhalation, which may not only enhance the

therapeutic effect against lung metastasis but also improve biological safety.

To prove our concept, herein, we designed an OPDEA-coated siPDK-containing copper-based MOF system (OMP) for the effective treatment of lung metastasis *via* regulating cuproptosis-mediated immunotherapy by inhalation administration (Fig. 1). Specifically, first, siPDK was loaded inside copper-based MOF through a facile one-pot protocol with high loading efficiency, named MP. The structural integrity of the MP scaffolds was pH dependent, a property that we leveraged to traffic siPDK payloads to the cytosol. Subsequently, OPDEA was legitimately coated on the surface of MP to obtain OMP, (where O represents OPDEA, M for copper-based MOF, and P for siPDK) (Fig. 1A). The obtained OMP administrated by aerosol inhalation route could effectively pass through the pulmonary mucosal layer and greatly enhance the accumulation and long-term retention in lung tissues. Subsequently, OMP was taken up by tumor cells and rapidly degraded to release Cu^{2+} within the acidic environment. Cu^{2+} was then converted to toxic Cu^+ by GSH to induce cuproptosis. Meantime, the co-released siPDK could effectively down-regulate PDK1 expression, suppress cancer cells glycolysis, leading to the decrease of intracellular ATP concentration and the following blocking of ATP7B. The combined effects could significantly lead to bidirectional amplification of cuproptosis. Subsequently, OMP-induced cuproptosis evoked ICD effect to enhance DCs maturation and in turn promote CD8^+ T cells proliferation to potentiate antitumor immunity. More importantly, OMP-mediated

cuproptosis increased the expression of membrane-associated PD-L1 (mPD-L1) and induced the secretion of soluble PD-L1 (sPD-L1) in tumor cells (Fig. 1B). Based on this observation, combined administration of OMP and aPD-L1 was evaluated as a means to promote CD8^+ T cells infiltration and remodel immunosuppressive TME. Collectively, an augmentative synergistic efficacy can be achieved by combining inhalable OMP-mediated cuproptosis with PD-L1 checkpoint blockade, which is promising to against lung metastasis with high efficiency and safety.

2. Materials and methods

2.1. Materials

N,N-Diethylaminoethyl methacrylate (DEA), 3-chloroperbenzoic acid (mCPBA), 2,2'-azobis (2-methylpropionitrile) (AIBN, 99%), *N*-hydroxysuccinimide (NHS, 99%), and *N,N'*-dicyclohexylcarbo-diimide (DCC, 99%) were bought from J&K Chemical (Beijing, China). 3-Maleimidopropionic acid and 4-cyano-4-(phenylcarbonothioylthio) pentanoic acid (CPADB) were purchased from Aladdin company (Shanghai, China). Cupric nitrate [$\text{Cu}(\text{NO}_3)_2$] and zinc nitrate hexahydrate [$\text{Zn}(\text{NO}_3)_2 \cdot 6(\text{H}_2\text{O})$] were purchased from Sinopharm Chemical Reagent Co., Ltd. (Shanghai, China). Glutathione (GSH) and 5,5'-dithiobis-(2-nitrobenzoic acid) (DTNB) were ordered from Sigma–Aldrich (Wisconsin, USA). RPMI 1640 medium, Dulbecco's modified Eagle's medium (DMEM),

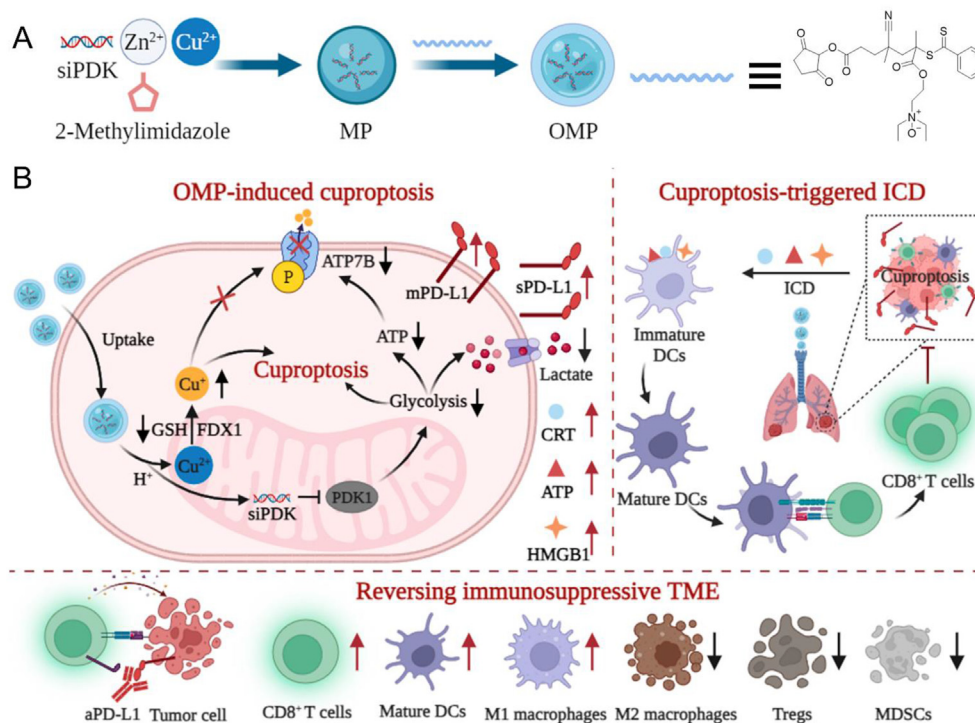


Figure 1 Schematic illustration of the mechanism of inhalable OMP-mediated cuproptosis activation for evoking strong anti-tumor immunity in lung metastasis. (A) Synthetic process of inhalable OMP nanoparticles. (B) The synergistic potency of inhalable OMP-induced cuproptosis combined with PD-L1 checkpoint blockade for provoking robust immune response, and further reshaping immunosuppressive TME. siRNA targeting pyruvate dehydrogenase kinase 1 (siPDK), membrane-associated PD-L1 (mPD-L1), soluble PD-L1 (sPD-L1), anti-PD-L1 antibodies (aPD-L1), immunogenic cell death (ICD), calreticulin (CRT), high mobility group box 1 (HMGB1), adenosine-5'-triphosphate (ATP), dendritic cells (DCs), myeloid-derived suppressor cells (MDSCs), regulatory T cells (Tregs), and tumor microenvironment (TME). This illustration was created with [BioRender.com](https://www.biorender.com).

penicillin–streptomycin, fetal bovine serum (FBS), and trypsin were purchased from Gibco Life Technologies (Grand Island, USA). Lysosome red fluorescent probe was obtained from Meilunbio Co., Ltd. (Dalian, China). Glucose content detection kit, ATP content detection kit, and anti-ATP7B polyclonal antibody-FITC were purchased from Biosharp Co., Ltd. (Hefei, China). DAPI, lactate content detection kit, and pyruvate dehydrogenase (PDH) activity detection kit were obtained from Beijing Solarbio Science & Technology Co., Ltd. (Beijing, China). β -Actin monoclonal antibody (AF5001), PD-L1 polyclonal antibody (AF7710), actin-tracker red, 3-(4,5-dimethylthiazole)-2,5-diphenyltetrazolium bromide (MTT), GSH assay kit, Alexa Fluor 488-labeled goat anti-rabbit IgG (H+L), and hematoxylin and eosin (H&E) staining kit were purchased from Beyotime (Shanghai, China). aPD-L1 antibodies (cat. no. BE0101) used for *in vivo* therapy were purchased from BIOXCELL Biotech Co. (New Hampshire, USA). Blanked siRNA, siPDK, FAM- and Cy5-labeled siPDK were purchased from Guangzhou RiboBio Co., Ltd. and Beijing Tsingke Biotech Co., Ltd. Cu^+ colorimetric assay kit was ordered from Elabscience Biotechnology Co., Ltd. (Wuhan, China). Coppersensor-1 (CS-1) was purchased from SAITONG Biotechnology Co., Ltd. (Beijing, China). PDK1 polyclonal antibody (18262-1-AP), CRT monoclonal antibody (10292-1-AP), and DLAT polyclonal antibody (13426-1-AP) were obtained from Proteintech Group, Inc. (Rosemont, USA). Lipoic acid (ab58724) and FDX1 (ab108257) were ordered from Abcam Ltd. (Cambridge, UK). ACO-2 (6571) was purchased from Cell Signaling Technology, Inc. (Massachusetts, USA). HMGB1 detection kit was obtained from YI FEI XUE Biotech Co., Ltd. (Nanjing, China). PD-L1, IL-6, IFN- γ , IL-12, TNF- α , and IL-10 ELISA Kit were ordered from Multisciences (Lianke) Biotech, Co., Ltd. (Hangzhou, China). B16F10 cells and Caco-2 cells were obtained from the cell bank of the Chinese Academy of Sciences (Shanghai, China). Six weeks old female C57BL/6J mice were obtained from Beijing Vital River Laboratory Animal Technology Co., Ltd. (Beijing, China). Animal experiments were approved by the Laboratory Animal Ethical and Welfare Committee of Chee-loo College of Medicine of Shandong University, and all animal procedures were performed in accordance with the guidelines of Institutional Animal Care and Use Committee (IACUC) of Shandong University (ethical approval number: ECSPSSDU2023-2-227).

2.2. Methods

2.2.1. Synthesis of *N,N*-diethylaminoethyl methacrylate (ODEA)
2-(Diethylamino) ethyl methacrylate (DEA, 0.93 g, 5 mmol) was dissolved in anhydrous CH_2Cl_2 (20 mL) in an ice bath. mCPBA (1.30 g, 0.75 mmol) was added portion-wise within 30 min with vigorous stirring. Afterward, the solution was allowed to warm to room temperature and stirred for another 2 h. After removing the solvent by evaporation, the residues were purified using a neutral alumina column, affording ODEA (0.82 g, yield: 79.6%) as an off-white waxy solid. ^1H NMR (400 MHz, CDCl_3) δ 6.16 (s, 1H), 5.61 (s, 1H), 4.74 (t, J = 3.4, 3.6 Hz, 2H), 3.47 (t, J = 9.4, 8.6 Hz, 2H), 3.31 (dd, J = 6.5, 7.4 Hz, 4H), 1.95 (s, 3H), 1.32 (t, J = 7.2, 6.8 Hz, 6H).

2.2.2. Synthesis of 2-cyano-5-(2,5-dioxopyrrolidin-1-yl)-5-oxopentan-2-yl benzodithioate (NHS-CPADN)
4-Cyano-4-(phenylcarbonothioylthio)pentanoic acid (CPADB, 1.40 g, 5 mmol) and *N*-hydroxysuccinimide (NHS, 0.58 g,

5 mmol) were co-dissolved in anhydrous CH_2Cl_2 (15 mL). Dicyclohexylcarbodiimide (DCC, 1.03 g, 5 mmol) was added to this solution and the reaction mixture was stirred at room temperature for 18 h. An insoluble white by-product was removed by filtration. The remaining solution was concentrated using a rotary evaporator, and the resulting liquid was purified by silica column chromatography using a mixed eluent comprising (PE:EA = 5:1). A red solid was isolated after evaporation of the solvent (1.67 g, yield: 92.3%). ^1H NMR (400 MHz, CDCl_3) δ 7.99–7.80 (m, 1H), 7.67–7.51 (m, 1H), 7.51–7.32 (m, 1H), 3.07–2.94 (m, 1H), 2.88 (d, J = 9.4 Hz, 2H), 2.80–2.67 (m, 1H), 2.57 (ddd, J = 9.4, 9.1, 6.2 Hz, 1H), 1.97 (s, 2H).

2.2.3. Synthesis of OPDEA

NHS-CPADN (36 mg, 100 μmol), ODEA (400 mg, 2 mmol), and AIBN (1.7 mg, 10 μmol) were dissolved in dried DMF (3 mL) and sealed in a flask under the protection of N_2 . The reaction was proceeded under 80 $^\circ\text{C}$ for 24 h. Then the solution was cooled down to room temperature and dialyzed against ethanol and water for 2 days. The final product of OPDEA (203.1 mg, yield: 48.8%) was obtained by freeze-drying. The number of ODEA monomeric units in OPDEA was about 10, determined by ^1H NMR.

2.2.4. Preparation of siPDK-encapsulating copper-based MOF (MP)

$\text{Cu}(\text{NO}_3)_2$ (12 mg), $\text{Zn}(\text{NO}_3)_2 \cdot 6\text{H}_2\text{O}$ (12 mg), and 60 μL of siPDK solution (100 $\mu\text{mol/L}$) were added to methanol (500 μL) (solution A). 2-Methylimidazole (33 mg) was dissolved in methanol (1 mL) (solution B). Under stirring, the solution B was slowly added into solution A and stirred for 20 min in an ice bath. After centrifugation, the product was washed three times with ethanol and H_2O . The obtained solid was dried under reduced pressure. The copper-based MOF and blank siRNA-encapsulating copper-based MOF were similarly synthesized. The sequence of siPDK was used as follows: 5'-GACAGAAUCCGUCGAGAGA dTdT-3' (sense); 5'-UCUCUCGACGGAUUCUGUC dTdT-3' (antisense). The blank siRNA sequences: 5'-UUCUCCGAACGUGUCACGUTT-3' (sense), 5'-ACGUGACACGUUCGGAGAATT-3' (antisense).

2.2.5. Preparation of OMP nanoparticles

OPDEA solution (2 mg/mL) was provided in bi-distilled H_2O . MP (2 mg/mL in H_2O) was added dropwise within 10 min, and the dispersion was allowed to stir for 20 min. Ultrasound was applied for 3 min, and the solution was again stirred for 20 min. The resulting particles were centrifuged at 12,000 rpm for 30 min (Z36HK, HermLe, DE) and washed twice with H_2O . OMP nanoparticles were stored in an aqueous stock solution. The size, zeta potential, and morphology of OMP were then measured by a Malvern Zetasizer Nano ZS90 (Malvern Instruments Ltd., UK) and transmission electron microscope (TEM, Hitachi H-600, Japan).

2.2.6. pH-Triggered siPDK and Cu^{2+} release from OMP

To evaluate the *in vitro* pH-sensitive release properties of siPDK and Cu^{2+} from OMP, siPDK was labeled with FAM fluorescent dye. OMP was incubated in PBS (pH 7.4, 6.8, and 5.5) at 37 $^\circ\text{C}$. At predetermined time intervals (0.5, 1, 1.5, 2, 3, 4, 6, 8, 16, and 24 h), 200 μL of particle solution was taken out and centrifuged at 12,000 rpm for 30 min, and 50 μL of the upper liquid was used for analysis of the release of FAM-labeled siPDK by a multimode plate reader (Tecan Infinite[®] 200 PRO, China). Fifty microliter of

the upper liquid was used for analysis of the release of Cu^{2+} by inductively coupled plasma mass spectra (ICP-MS).

2.2.7. OMP-mediated GSH depletion and Cu^+ generation

For GSH depletion, OMP with different concentrations (0, 10, 25, 50, and 100 $\mu\text{g}/\text{mL}$) were mixed with GSH solution (10 mmol/L) at pH 5.5 for 20 min at 37 °C, respectively. DTNB solution (2.5 mg/mL) was then added to each solution, followed by 5 min of stirring. After that, the absorbance at 412 nm was recorded via a multimode plate reader. For Cu^+ generation, OMP suspension (100 $\mu\text{g}/\text{mL}$) were treated with different concentration of GSH (0, 2.5, 5, 10, and 20 mmol/L) at pH 5.5 for 1 h at 37 °C. The fluorescence intensity at 608 nm ($\text{Ex} = 365 \text{ nm}$) was recorded by a microplate plate reader.

2.2.8. Cell culture

B16F10 cells and Caco-2 cells were cultured in complete RPMI 1640 cell culture medium or DMEM culture medium containing 10% fetal bovine serum (FBS), 100 U/mL of penicillin, and 100 U/mL of streptomycin. Cell cultures were maintained at 37 °C in 5.0% CO_2 atmosphere.

2.2.9. Cellular uptake

To assess the cellular uptake of siPDK-loaded nanoformulations, FAM-MP and FAM-OMP were formed by encapsulating FAM-labeled siPDK. B16F10 cells were seeded on 35-mm sterile glass bottom culture dishes (3×10^5 cells) and cultured for 24 h. Then, FAM-siPDK, FAM-MP, and FAM-OMP were incubated with B16F10 cells for 0.5, 1, 2, and 4 h. Next, the cells were washed three times with PBS, and the cell nuclei were stained with DAPI for 20 min. Images and data were acquired with confocal laser scanning microscopy (CLSM, Dragonfly 200, Andor, UK) and flow cytometry (Beckman CytoFLEX S, USA).

2.2.10. In vitro cell cytotoxicity assay

The cytotoxicity of B16F10 cells was evaluated using MTT assay. In brief, B16F10 cells were seeded into 96-well plates (4×10^3 cells/well) for 24 h. Subsequently, MN, MP, OMN, and OMP were administrated at concentrations of 3.75, 7.5, 15, 30, 60, and 90 $\mu\text{g}/\text{mL}$ (other groups were converted to the same amount of siPDK or Cu^{2+}). After 24-h incubation, the B16F10 cells were incubated with 10 μL of MTT solution in each well at 37 °C for 4 h. And then the absorbance of solution at a wavelength of 490 nm was detected by a microplate reader. The cytotoxicity of various nanoparticles in Caco-2 cells and bone marrow-derived DCs (BMDCs) were measured in the same way.

To measure the B16F10 cells viability in the presence of different inhibitors, cells were seeded into 96-well plates for 24 h. Then, OMP (90 $\mu\text{g}/\text{mL}$) was subsequently added to each well separately. Ferroptosis inhibitors (ferrostatin-1, 10 mmol/L), necroptosis inhibitors (necrostatin-1, 20 mmol/L), oxidative stress inhibitors (*n*-acetylcysteine, 5 mmol/L), apoptosis inhibitors (Z-VAD-FMK, 30 mmol/L), and copper chelator tetrathiomolybdate (TTM, 20 mmol/L) were added. The cytotoxicity was then measured quantitatively using the standard MTT assay after 24 h.

2.2.11. Intracellular PDH activity, glucose, ATP, and extracellular lactate determination

For PDH activity quantification, B16F10 cells were seeded into 6-well plates at a density of 3×10^5 cells/well for 24 h. Then, cells were treated with PBS, MN, MP, OMN, and OMP (60 $\mu\text{g}/\text{mL}$), other groups were converted to the same amount of Cu^{2+} or

siPDK) for 24 h at 37 °C. The cells were first homogenized to get lysate and then added to the working solution according to the manufacturer's protocols. The glucose and ATP were quantified with a similar method. For lactate contents quantification, B16F10 cells were seeded into 6-well plates at a density of 3×10^5 cells/well for 24 h. After 24 h, cells were treated with PBS, MN, MP, OMN, and OMP (60 $\mu\text{g}/\text{mL}$), other groups were converted to the same amount of Cu^{2+} or siPDK) for 24 h at 37 °C. The media was directly taken out for lactate determination according to the manufacturer's protocols.

2.2.12. Evaluation of intracellular ATP7B levels

B16F10 cells were seeded into 6-well plates. Then the cells were treated with PBS, MN, MP, OMN, and OMP (60 $\mu\text{g}/\text{mL}$), other groups were converted to the same amount of Cu^{2+} or siPDK) for 24 h. Thereafter, ATP7B levels were determined by using FITC-conjugated anti-ATP7B polyclonal antibodies. Briefly, B16F10 cells were washed with PBS and then incubated with anti-ATP7B polyclonal antibody-FITC (1:100) overnight at 4 °C. Following the incubation, the cells were further treated with DAPI for 20 min, washed 3 times with PBS, and collected for CLSM and flow cytometry analysis.

2.2.13. Intracellular GSH assay

The GSH assay kit was applied to investigate the cellular GSH levels in B16F10 cells. B16F10 cells were seeded into 6-well plates at a density of 3×10^5 cells/well for 24 h. Then the cells were treated with PBS, MN, MP, OMN, and OMP (60 $\mu\text{g}/\text{mL}$), other groups were converted to the same amount of Cu^{2+} or siPDK). After 24 h, the intracellular GSH contents were determined by GSH assay kit according to the manufacturer's protocol.

2.2.14. Determination of intracellular Cu^+ contents

The concentrations of intracellular Cu^+ were evaluated using Cu^+ colorimetric assay kit and Cu^+ -responsive probe Coppensor-1 (CS-1). B16F10 cells were seeded on 6-well plates (3×10^5 cells/well) followed by incubation for 24 h. Then, PBS, MN, MP, OMN, and OMP (60 $\mu\text{g}/\text{mL}$), other groups were converted to the same amount of Cu^{2+} or siPDK) were administrated. Afterward, the cells were collected at 24 h after incubation, followed by ultrasonic cell disruption. Finally, the Cu^+ amounts were determined using Cu^+ colorimetric assay kit according to the manufacturer's protocols. For Cu^+ -responsive probe Coppensor-1 (CS-1) to detect the concentrations of Cu^+ , B16F10 cells were seeded into 6-well plates at a density of 3×10^5 cells/well for 24 h. Subsequently, different nanoparticles were incubated with B16F10 cells for 24 h. Next, the cells were washed three times with PBS, and the cells were stained with CS-1 (5 $\mu\text{mol}/\text{L}$) for 5 min. Data were acquired with flow cytometry.

2.2.15. Western blot analysis

B16F10 cells were seeded into 6-well plates at a density of 3×10^5 cells/well for 24 h. For PDK1, ACO-2, Lip-DLAT, DLAT, FDX1, and PD-L1 assays, the cells were treated with PBS, MN, MP, OMN, and OMP (60 $\mu\text{g}/\text{mL}$), other groups were converted to the same amount of Cu^{2+} or siPDK) for 24 h, respectively. After that, the cells were washed thoroughly with ice-cold PBS and then lysed in radioimmunoprecipitation assay (RIPA) lysis buffer (P0013B, Beyotime). The lysates were centrifuged at 4 °C at 12,000 rpm for 30 min. Protein concentration was quantified using the protein concentration determination kit (P0011, Beyotime). A total of 20 μg protein/lane was separated using 7.5% or 12.5%

SDS-PAGE. Separated proteins were transferred to a polyvinylidene fluoride (PVDF) membrane and blocked with 5% skim milk powder for 2 h at room temperature. Next, the membrane was incubated overnight with primary antibodies. The β -actin proteins were labeled by β -actin antibody (1:8000, 42 kDa) as loading control for whole-cell lysate, and PDK1, ACO-2, Lip-DLAT, DLAT, FDX1, and PD-L1 proteins were detected by PDK1 antibody (1:5000, 46 kDa), ACO-2 antibody (1:2000, 85 kDa), Lipoic acid antibody (1:6000, 71 kDa), DLAT antibody (1:5000, 70 kDa), FDX1 (1:5000, 14 kDa), and PD-L1 antibody (1:4000, 43 kDa), respectively. After that, the membrane was further treated with the horseradish peroxidase (HRP)-labeled goat anti-rabbit secondary antibody (A0208, Beyotime) for 1 h at room temperature. Finally, protein bands were visualized using an enhanced chemiluminescence system. The protein expressions were evaluated by analyzing the gray levels.

2.2.16. Evaluation of DLAT aggregation

B16F10 cells were seeded on 35-mm sterile glass bottom culture dishes (3×10^5 cells) and cultured for 24 h. Then, PBS, MN, MP, OMN, and OMP (60 μ g/mL, other groups were converted to the same amount of siPDK or Cu^{2+}) were respectively incubated with B16F10 cells for 24 h. After that, the cells were sequentially fixed with 4% paraformaldehyde, incubated with the DLAT antibody (1:100) at 4 °C overnight, treated with Alexa Fluor 488 anti-rabbit secondary antibody at room temperature for 1 h, stained with DAPI for 20 min, and imaged by CLSM.

2.2.17. In vitro investigation of ICD effect and DCs maturation

To evaluate the capacity of OMP-mediated cuproptosis-induced ICD effect, B16F10 cells were treated with PBS, MN, MP, OMN, and OMP (60 μ g/mL, other groups were converted to the same amount of siPDK or Cu^{2+}) for 24 h. Then, the treated cells were fixed using 4% paraformaldehyde and permeabilized using 0.3% Triton for 30 min. Afterward, B16F10 cells were incubated with calreticulin (CRT) antibody (1:100) at 4 °C overnight, followed by further incubation with Alexa Fluor 488-conjugated secondary antibody for another 1 h at room temperature and staining using DAPI for 20 min. Finally, the cells were rinsed with PBS three times before observation under CLSM. To investigate HMGB1 and ATP levels, 100 μ L of the culture media of B16F10 cells were collected after treatment with different nanoformulations for 24 h according to the manufacturer's protocol.

To analyze DCs maturation *in vitro*, bone marrow-derived DCs (BMDCs) were obtained from the femurs and tibiae of six-week-old female C57BL/6J mice. After the lysis of red blood cells, the collected cells were incubated with 1640 medium and 20 ng/mL granulocyte-macrophage colony-stimulating factor (GM-CSF) and 10 ng/mL IL-4. The culture medium was half replaced every 2 days. On Day 8, the non-adherent and loosely adherent cells were collected as inactivated BMDCs. B16F10 cells were pretreated with PBS, MN, MP, OMN, and OMP (60 μ g/mL, other groups were converted to the same amount of siPDK or Cu^{2+}) for 24 h. Then, BMDCs (5×10^5 cells/well) and the supernatant of the pretreated B16F10 cells were co-cultured. The maturation of the BMDCs was determined using flow cytometry after staining with anti-CD11c-APC, anti-CD86-PE-Cy5.5, and anti-CD80-FITC. Then, the levels of IL-6 and TNF- α in the culture medium were measured by ELISA kits.

2.2.18. Evaluation of membrane-associated PD-L1 and soluble PD-L1 expression

To evaluate membrane-associated PD-L1 expression, B16F10 cells were seeded on 6-well plates (3×10^5 cells/well) and incubated for 24 h. Afterwards, B16F10 cells were treated with PBS, MN, MP, OMN, and OMP (60 μ g/mL, other groups were converted to the same amount of siPDK or Cu^{2+}) for 24 h. Then, the cells were collected, stained with FAM-aPD-L1 for 30 min at room temperature, and analyzed using flow cytometry.

For evaluation of soluble PD-L1 secretion, B16F10 cells were seeded on 6-well plates (3×10^5 cells/well) and incubated for 24 h. Then, different nanoformulations were incubated with B16F10 cells for 24 h. After that, the media was directly taken out for soluble PD-L1 determination using the PD-L1 ELISA kit according to the manufacturer's protocols.

2.2.19. In vivo tissue distribution of inhalation of OMP

To investigate the *in vivo* behaviour, siPDK was labeled with a red fluorescence probe (Cy5) and encapsulated in the nanoformulations, named Cy5-MP and Cy5-OMP. A total of 27 female C57BL/6 mice were randomly divided into three groups, including the Cy5-MP (inh), Cy5-OMP (i.v.), and Cy5-OMP (inh) (where inh represents inhalation, i.v. for intravenous injection). Cy5-MP (inh) and Cy5-OMP (inh) groups were administered intratracheally by a microsyringe (MSA-250, PennCentury, USA). Under the guidance of the small animal laryngoscope (BJ-L, BioJane, China), the tip of the microsyringe is carefully placed into the trachea, followed by *in situ* tracheal administration with an injection rod. At 1, 6, and 24 h after inhalation of different nanoparticles (5 mg/kg), mice were sacrificed, and their heart, lungs, liver, spleen, and kidney were collected for imaging assessments by an IVIS spectrum *in vivo* imaging system (IVIS, PerkinElmer, USA). Furthermore, the lungs isolated at 1 h were made into sections for assessments of the lung accumulation function by CLSM (VS120, Olympus, Japan).

2.2.20. In vivo anti-metastatic effect of OMP combined with PD-L1 checkpoint blockade

Mice-bearing B16F10 lung melanoma metastasis was selected as a typical lung metastatic tumor model to evaluate the anticancer activity of the combination of OMP (inh) + aPD-L1 (i.v.). Metastatic lung tumor model was established by intravenous injection (i.v.) of 3×10^5 B16F10 cells. Seven days after i.v. injection of cancer cells, mice were randomly divided into five groups, including 1: PBS (inh), 2: aPD-L1 (i.v.), 3: OMP (i.v.), 4: OMP (inh), and 5: OMP (inh) + aPD-L1 (i.v.). OMP (5 mg/kg) was inhaled or injected intravenously for four times every 4 days and aPD-L1 antibodies (3 mg/kg) were applied together after inhalation of OMP for 24 h to achieve the best therapeutic efficiency. The therapeutic results were mainly evaluated by the number of lung metastasis foci and the survival rates of mice. The toxicity of nanoformulations was evaluated by the body weight of mice. On Day 18, lungs and sera were collected from the sacrificed mice. The obtained lung tissues were used for qRT-PCR analysis, hematoxylin and eosin (H&E) staining analysis, DLAT and CRT immunofluorescence assay. Moreover, the analysis of immune effects was studied by flow cytometry and ELISA assay.

The first was flow cytometry analysis. For analysis of dendritic cells (DCs) maturation, lymphocytes were extracted

from tumor-draining lymph nodes, and then stained with anti-CD45-APC-Cy7, anti-CD11c-APC, anti-CD86-PE-Cy5.5, and anti-CD80-FITC for 30 min at room temperature, followed by analysis using flow cytometry. For analysis of immune-attacking cells infiltration, the lungs were harvested, cut into small pieces, and digested by dissociation buffer with 1640 medium containing 100 U/mL of hyaluronidase, 1 mg/mL of collagenase IV and 30 U/mL of DNase for 1 h at 37 °C. The suspensions were filtered through 75- μ m filters to obtain single cell suspension. To estimate the CD8⁺ T cells (CD45⁺CD3⁺CD8⁺ T cells) infiltration and proportion in metastatic lungs, the cell suspensions were stained with anti-CD45-APC-Cy7, anti-CD3-FITC, and anti-CD8a-PE for 30 min. For M1 macrophages and M2 macrophages (CD45⁺F4/80⁺CD86⁺CD206⁻ M1 macrophages, CD45⁺F4/80⁺CD86⁻ M2 macrophages) evaluation, the cell suspensions were labeled by anti-CD45-APC-Cy7, anti-F4/80-Brilliant violet 421 (BV421), anti-CD86-PE-Cy5.5, and anti-CD206-PE-Cy7. For analysis of immune-suppressive myeloid-derived suppressor cells (MDSCs) (CD45⁺CD11b⁺Gr-1⁺ MDSCs) in metastatic lungs, anti-CD45-Cy7, anti-CD11b-APC, and anti-Gr-1-PE were applied to stain the single cell suspensions for 30 min. For analysis of immune-suppressive cells regulatory T lymphocytes (Tregs) (CD45⁺CD4⁺Foxp3⁺ Tregs), single cell suspensions were firstly stained with anti-CD45-Cy7 and anti-CD4-Percp/Cy5.5 for 30 min and further handled with True-Nuclear™ Perm buffer, and then stained with anti-Foxp3-Brilliant violet 421 (BV421) antibody for 60 min.

Next is ELISA and mRNA analysis. Lungs collected from mice were homogenized in lysis buffer, and then centrifuged at 12,000 \times *g* for 15 min. The supernatant was collected and the concentrations of IL-10, IL-6, IL-12, TNF- α , and IFN- γ were measured using ELISA kits according to the manufacturer's instructions. The PDK1 and PD-L1 mRNA expression levels were quantified using the qRT-PCR technology, as described above. The following primers were used (5' \rightarrow 3'). M- β -actin-S, CACCCGCGAGTACAACCTTC, M- β -actin-A, CCCATACCC ACCATCACACC; M-PDK1-S, AATACAGCCGCAGGTTGG CC, M-PDK1-A, CCGAAGTCCAGGAAGTCTT; M-PD-L1-S, TCAATGCCCCATACCGCAAA, M-PD-L1-A, TCTCTCCAC TCACGGGTT. RNA expression was normalized to β -actin expression in the relevant untreated controls. Besides, the blood of the mice was collected on Day 18 for blood biochemistry analysis.

2.2.21. Statistical analysis

All statistical analyses were performed with GraphPad Prism 8 software. Data are expressed as mean \pm standard deviation (SD), and the differences between groups assessed using two-sided Student's *t*-test or one-way ANOVA with Tukey's *post hoc* test. Statistical differences were defined as: ns means no significant difference, **P* < 0.05, ***P* < 0.01, ****P* < 0.001, *****P* < 0.0001.

3. Results and discussion

3.1. Synthesis, characterization, and cellular uptake of OMP

The water-soluble polyzwitterionic OPDEA was synthesized and characterized, as shown in (Supporting Information Scheme S1 and Figs. S1–S3). OPDEA was prepared by a three-step

procedure using reversible addition–fragmentation chain transfer (RAFT) polymerization. The OPDEA weight was controlled to be \sim 3 kDa, as determined using ¹H NMR. The siPDK-encapsulating copper-based MOF (MP) was fabricated by a simple one-step method, by mixing siPDK, 2-methylimidazole, Cu(NO₃)₂, and Zn(NO₃)₂·6H₂O in methanol under stirring for 20 min³¹. For the coating process, OPDEA was mixed with the MP at the weight ratios of 1:1 and stirred vigorously for 20 min. Last, the OPDEA-coated MP (OMP) were isolated by centrifugation (Fig. 1A). The TEM imaging indicated that the copper-based MOF without siPDK loading possessed an average diameter of 80.2 \pm 0.5 nm (Fig. 2A). DLS measurement displayed the average hydrodynamic size of 77.9 \pm 5.7 nm (Fig. 2B). The MP nanoparticles were slightly larger than unloaded copper-based MOF, with an average hydrodynamic size of 99.5 \pm 6.7 nm, and OPDEA coating further increased their size, with the final OMP nanoformulation exhibiting an average hydrodynamic diameter of approximately 147.4 \pm 2.1 nm (Fig. 2B). Moreover, while loading of the negatively charged siPDK payload slightly decreased the surface zeta potential compared with unloaded copper-based MOF, the OPDEA coating had a profound impact on shielding the positively charged MP core, resulting in OMP nanoparticles that were considered neutral in charge (Fig. 2C). Both the size and surface zeta potential data suggested successful coating of the OPDEA around the MP nanoparticles, and the core–shell morphology of the OMP nanoparticles was confirmed by TEM (Fig. 2A). Moreover, OMP was stable in the fetal bovine serum for up to a week (Supporting Information Fig. S4). In terms of siPDK loading, the encapsulation efficiency was quantified by incorporating FAM-labeled siPDK at increasing concentrations. The encapsulation efficiency of the siPDK was 95.0 \pm 1.0%, at the weight ratios of 1:20 (siPDK: copper-based MOF) (Supporting Information Fig. S5). The favorable loading exhibited by the copper-based MOF was likely attributed to strong electrostatic interactions between the framework's metal nodes and the siPDK's backbone phosphates, as well as physical confinement within the nanoporous structure. Moreover, OMP protected siPDK from RNase A digestion, whereas naked siPDK was degraded rapidly within 90 min (Supporting Information Fig. S6). Furthermore, the Cu and P contents in OMP were determined by ICP-MS to be 12.3% and 0.236%, respectively.

To explore the pH-responsive drug release ability, the obtained OMP nanoparticles were dispersed into phosphate buffer saline (PBS) solutions with different pH values (7.4, 6.8, and 5.5, which simulated the pH of normal cells, tumor microenvironment, and the inside of tumor cells, respectively). As expected, only a minimal amount of siPDK release (less than 20.0% over 24 h) was observed at pH 7.4, suggesting a relatively good chemical stability, while OMP displayed a considerable burst siPDK release (more than 90.0% over 24 h) at pH 5.5 (Fig. 2D). And the release curves of Cu²⁺ showed a similar trend. Under mildly acidic condition (pH 5.5), the release rate of Cu²⁺ was 91.2% at 24 h. However, it was 19.5% only under pH 7.4 condition (Fig. 2E). This pH-dependent property of OMP suggested that the siPDK could be protected within the nanoparticulate structure until after cellular internalization, upon which the mildly acidic environment of the endosomes would trigger siPDK release. Therefore, the endosomal escape of the OMP was investigated. In B16F10 cells treated with OMP, the overlap between the red fluorescence of Lyso-tracker red and the green fluorescence of FAM-labeled siPDK was reduced

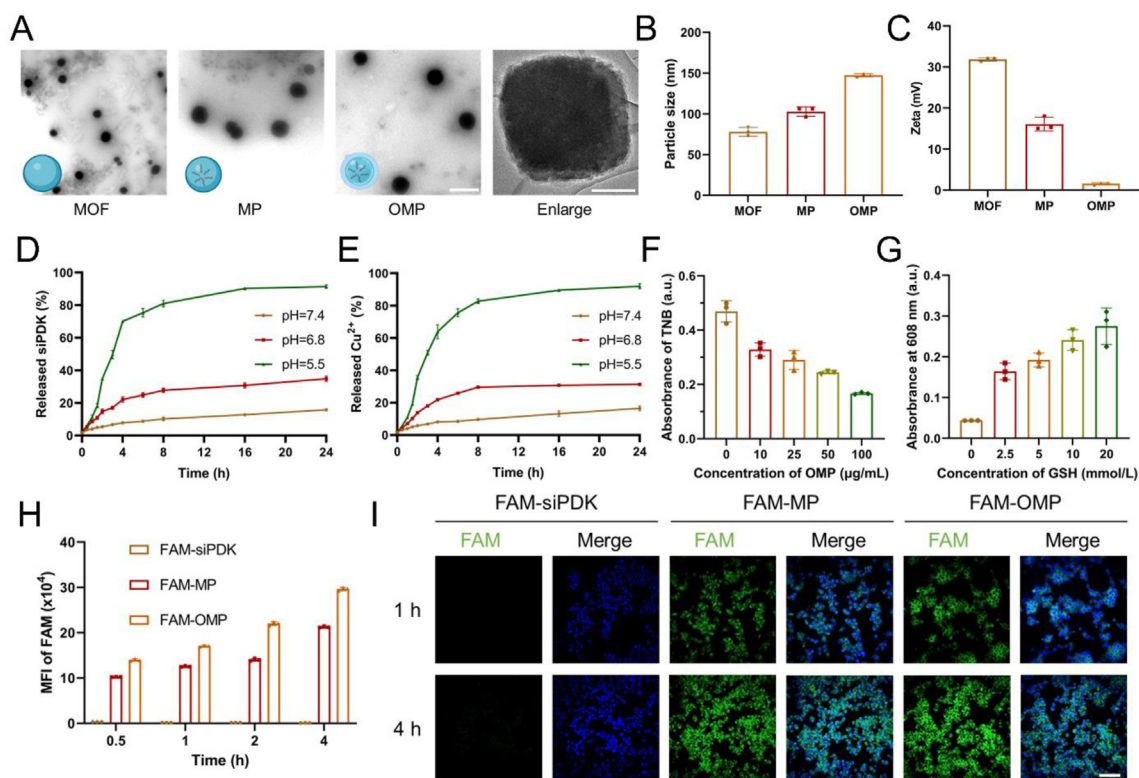


Figure 2 Synthesis, characterization, and cellular uptake of OMP. (A) TEM images of MOF, MP, and OMP (scale bar: 200 nm) and enlarged OMP TEM image (scale bar: 50 nm). (B) Size distribution and (C) zeta potential of MOF, MP, and OMP using DLS. (D) siPDK and (E) Cu²⁺ release curves of OMP at pH 7.4, 6.8, and 5.5 over time. (F) Absorbance of TNB solutions at 412 nm after treatment with different concentrations of OMP. (G) Evaluation of GSH-triggered generation of Cu⁺. The fluorescence intensity at 608 nm of OMP after incubation with different concentrations of GSH (Ex = 365 nm). (H) Semi-quantification of intracellular uptake of FAM-OMP by B16F10 cells at different time points. (I) Representative CLSM images of B16F10 cells after incubation with FAM-OMP for 1 and 4 h. Cell nuclei were stained with DAPI (blue). Scale bar: 100 μm. Data are shown as mean ± SD (*n* = 3).

when the incubation time reached 4 h, indicating the successful escape of siPDK from endosomes (Supporting Information Fig. S7).

GSH-mediated reduction of released Cu²⁺ into Cu⁺ species is the prerequisite to trigger cuproptosis. We thus evaluated the GSH-depleting ability of OMP by using 5,5'-dithiobis-(2-nitrobenzoic acid) (DTNB) as the probe, which can react with GSH to generate 2-nitro-5-thiobenzoic acid (TNB) with an absorbance at 412 nm³². Clearly, the absorbance of TNB decreased obviously with increasing Cu²⁺ concentration in OMP under acidic condition (Fig. 2F), reasonably attributing to pH-triggered Cu²⁺ release and subsequent reduction into Cu⁺. Subsequently, the GSH-triggered generation of Cu⁺ was verified by the fluorescence spectroscopy due to the ligand–metal charge transfer between GSH and copper³³. The intensity of Cu⁺ at 608 nm notably increased with the interaction with GSH, revealing the reduction of Cu²⁺ to Cu⁺ during GSH depletion (Fig. 2G).

According to researches, OPDEA exhibits phospholipid affinity, which fits the need for cellular uptake^{34,35}. To investigate whether OPDEA decoration could promote the cellular uptake of OMP in B16F10 cells, siPDK was labeled with a green fluorescence probe (FAM). On the one hand, the change of fluorescence intensity over time in B16F10 cells treated with FAM-OMP was semi-quantitatively studied by flow cytometry.

The results showed that the green fluorescence intensity of OMP in B16F10 cells at 4 h was 299.5 and 1.4 times higher than that of siPDK and MP, respectively. The above results indicated that OMP with OPDEA surface could be taken up more efficiently by B16F10 cells (Fig. 2H). On the other hand, the green fluorescence intensity in B16F10 cells at 1 and 4 h was visualized by confocal laser microscopy (CLSM). The results unveiled that OMP had the strongest green fluorescence intensity in B16F10 cells (Fig. 2I). Taken together, OMP could be efficiently taken up by B16F10 cells.

3.2. Mechanism of OMP-mediated cuproptosis

In normal cells, glucose enters mitochondria and usually undergoes mitochondrial respiration *via* TCA cycle. In contrast, for cancer cells, the TCA cycle is shut off and the glucose metabolism is mainly through glycolysis that limits the occurrence of cuproptosis. The activated glycolysis in cancer cells is mainly due to the highly expressed PDK1 that reduces the PDH activity and inhibits pyruvate to be converted to acetyl-CoA for TCA cycle¹³. To determine whether OMP could down-regulate PDK1 expression for metabolic regulation, we used Western blot and immunofluorescence analysis to visualize the PDK1 expression. The experiment is divided into five groups: control (PBS), MN, MP, OMN, and OMP (where O for OPDEA, M represents

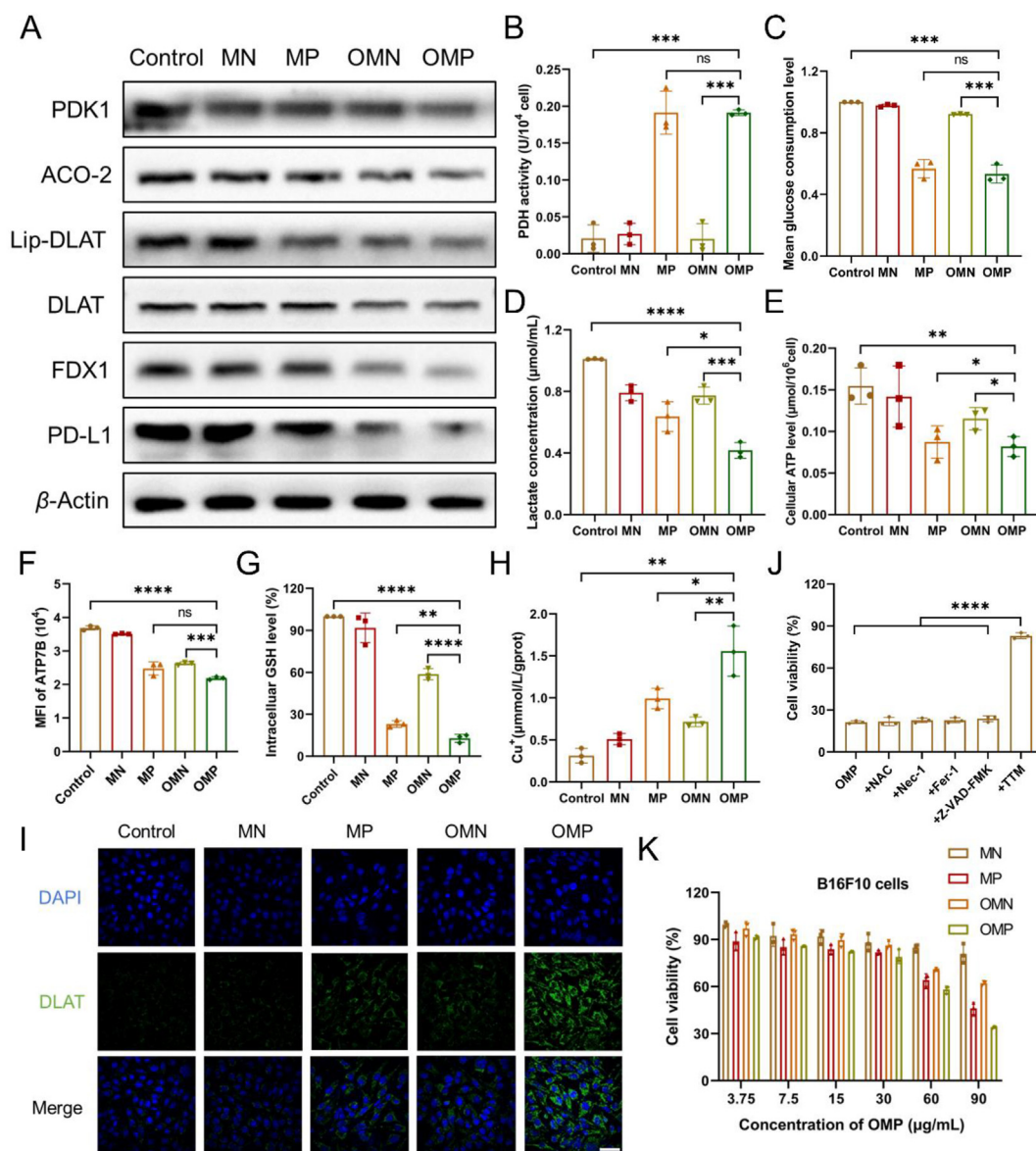


Figure 3 Studies on the OMP-induced cuproptosis *in vitro*. (A) Western blot analysis of B16F10 cells on the expressions of PDK1, ACO-2, Lip-DLAT, DLAT, FDX1, and PD-L1 after 24 h incubation with various nanoparticles. (B–E) Metabolic alterations in (B) PDH activity, (C) glucose consumption, (D) extracellular lactate, and (E) intracellular ATP production in B16F10 cells after various treatments for 24 h. (F) Semi-quantification of ATP7B expression in B16F10 cells with various treatments. (G) Intracellular GSH contents after various treatments. (H) The contents of Cu⁺ from B16F10 cells after treated with various nanoparticles for 24 h. (I) DLAT immunofluorescence images of B16F10 cells after different treatments for 24 h. Scale bar: 20 μm. (J) Relative viabilities of B16F10 cells treated with OMP only or plus with *N*-acetylcysteine (NAC), necrostatin-1 (Nec-1), ferrostatin-1 (Fer-1), Z-VAD-FMK and tetrathiomolybdate (TTM), respectively. (K) The viability of B16F10 cells after treated with various nanoparticles for 24 h. Data are shown as mean ± SD (*n* = 3). ns means no significant difference, **P* < 0.05, ***P* < 0.01, ****P* < 0.001, *****P* < 0.0001.

copper-based MOF, N refers to blank siRNA, and P for siPDK). B16F10 cells treated with OMP exhibited obvious PDK1 inhibition compared with control, MP, and OMN groups. The level of PDK1 in OMP group was 0.57-, 0.75-, and 0.63-fold compared with control, MP, and OMN groups, respectively (Fig. 3A and Supporting Information Fig. S8). The immunofluorescence of PDK1 in OMP group also exhibited the lowest fluorescence intensity (Supporting Information Fig. S9). Moreover, OMP could effectively decrease PDK1 expression in B16F10 cells in a concentration-dependent manner (Supporting

Information Fig. S10A and S10B). In contrast, no PDK1 down-regulation was observed using a naked siPDK. These results demonstrated that OMP could effectively down-regulate PDK1 expression. Subsequently, the PDH activity was measured after co-incubated the B16F10 cells with different nanoparticles for 24 h. The PDH activity was significantly increased by OMP treatment (increased by 9.2 and 9.0 times of the control and OMN groups, respectively) (Fig. 3B). To evaluate the metabolic regulation in B16F10 cells caused by OMP nanoformulations, the glucose consumption and lactate secretion

were analyzed. Due to the excellent PDH modulation capability, OMP efficiently decreased glucose consumption level (1.9-fold reduction compared to the control group) and extracellular lactate content (decreased by 2.4-fold of the control group) (Fig. 3C and D). Moreover, the intracellular ATP concentration in OMP group was 1.9 times lower than the control group, which suggested that OMP could effectively refrain the intracellular ATP generation (Fig. 3E). Taken together, these results collectively demonstrated the OMP could decrease PDK1 expression for inhibiting glycolysis, which would sensitize cancer cells to cuproptosis.

Owing to the restricted ATP supply, we then explored the effects of OMP on the expressions of ATP7B, which is the major Cu^+ transmembrane transporter to export Cu^+ out of cells relies heavily on ATP as energy. As shown in Fig. 3F and Supporting Information Fig. S11, the expression of ATP7B in the OMP group was prominently down-regulated compared with the control group. Meanwhile, intracellular GSH levels were studied since it can convert Cu^{2+} into toxic Cu^+ to induce cuproptosis. Compared with the high level of GSH in control group, the GSH contents of B16F10 cells were significantly decreased after treated with MP and OMP (Fig. 3G). Subsequently, the intracellular Cu^+ contents after various treatments were detected by using a Cu^+ colorimetric assay kit and Cu^+ -responsive probe Coppensor-1 (CS-1) (Fig. 3H and Supporting Information Fig. S12). These results showed that the intracellular Cu^+ contents were sharply elevated after treated with OMP for 24 h and increased by 4.6 and 2.2 times compared to those in control and OMN groups, respectively. These above results indicated that high levels of GSH in tumor cells could reduce Cu^{2+} from OMP to toxic Cu^+ , which would effectively induce cancer cells cuproptosis. These phenomena should be ascribed to the better cellular uptake and down-regulation of ATP7B expression. Subsequently, we explored the cuproptosis-related proteins expression and DLAT oligomerization immunofluorescence in B16F10 cells treated with different nanoparticles for 24 h. On the one hand, we performed the Western blot analysis of Fe-S cluster-containing proteins (ACO-2 and FDX1), lipoylated protein (Lip-DLAT), and DLAT, which played key roles in regulating cuproptosis and their loss was one of the hallmarks of cuproptosis. The expression of ACO-2, Lip-DLAT, DLAT, and FDX1 in the OMP group were 0.50-, 0.64-, 0.67-, and 0.46-fold of those in the control group, respectively (Fig. 3A and Fig. S8). Moreover, the levels of ACO-2, Lip-DLAT, DLAT, and FDX1 in the OMP group were 0.75-, 0.84-, 0.85-, and 0.73-fold of those in the OMN group, respectively. On the other hand, as shown in Fig. 3I, both MP and OMP groups showed increased degrees of DLAT aggregation, and the OMP group had a higher degree of DLAT aggregation. These results demonstrated that OMP possessed excellent ability to induce B16F10 cells cuproptosis by the synergistic effect of inhibiting glycolysis and suppressing ATP7B expression.

It has been reported that cuproptosis was a cell death mechanism distinct from known cell death pathways and couldn't be inhibited by the inhibitors of the above cell death methods. Therefore, B16F10 cells were incubated with inhibitors of known cell death mechanisms, including oxidative stress inhibitors (*n*-acetylcysteine), necroptosis inhibitors (necrostatin-1), ferroptosis inhibitors (ferrostatin-1), and apoptosis inhibitors (Z-VAD-FMK). All inhibitors failed to abolish Cu^+ -induced cell death, further confirming that cuproptosis was a unique form of death (Fig. 3J). Conversely, tetrathiomolybdate (TTM) significantly inhibits cell susceptibility to OMP, because which could chelate with Cu^+ .

This result suggested that cuproptosis was mainly dependent on the accumulation of intracellular Cu^+ . Afterward, the cytotoxicity of different nanoparticles towards B16F10 cells was evaluated by MTT assay. With the increase of concentrations, MN showed moderate cytotoxicity to B16F10 cells (Fig. 3K), while MP showed increased cytotoxicity since the loaded siPDK which could significantly regulate intracellular glucose metabolism pattern and down-regulate ATP7B expression, and subsequently sensitize B16F10 cells to cuproptosis. Furthermore, the OMP-treated cells showed lower cell viabilities than MP-treated ones, further confirming that the functionalization of OPDEA increased cellular uptake and tumor-killing ability of OMP. These results further indicated OMP could sensitize B16F10 cells to cuproptosis and effectively induce cuproptosis-mediated cancer cells death.

3.3. OMP-induced cuproptosis dependent-ICD *in vitro*

Owing to the outstanding performance of OMP-induced cuproptosis in B16F10 cells, the role of OMP-mediated cuproptosis in the promotion of ICD was further explored (Fig. 4A). ICD is characterized by releasing DAMPs from dying tumor cells, such as CRT, HMGB1, and ATP. CRT acted as an "eat me" signal when exposed on the membrane surface of tumor cells and motivated DCs maturation and CD8^+ T cells activation. Thus, we determined whether CRT was exposed on the B16F10 cells membrane surface after co-incubated with different nanoparticles for 24 h. The immunofluorescence assay results were shown in Fig. 4B, more cell-surface exposure of CRT was detected in the OMP group. Encouraged by the above result, two other ICD biomarkers, HMGB1 and ATP, were also evaluated (Fig. 4C and D). The OMP group induced significantly increased extracellular secretion of HMGB1 and ATP compared with the control group that confirmed the release of DAMPs. These findings suggested that OMP-mediated cuproptosis could evoke ICD to induce the release of DAMPs, which could facilitate the subsequent immune response.

To verify the adaptive immunity introduced by OMP-mediated cuproptosis, the maturity of DCs as a crucial hallmark was investigated *in vitro* by co-incubating bone-marrow-derived DCs (BMDCs) with the supernatant of B16F10 cells subjected to different treatments. As shown in Fig. 4E and F, the OMP group showed an augmented increase in DCs maturation (3.6-fold relative to the control, 1.4-fold relative to the MP group, and 2.0-fold relative to the OMN group), indicating cuproptosis-evoked ICD effect could efficiently promote DCs maturation. Moreover, the production of mature DCs-related cytokines including IL-6 and $\text{TNF-}\alpha$ were investigated *via* ELISA assay, and OMP group also showed the most IL-6 and $\text{TNF-}\alpha$ contents (Fig. 4G and H). Notably, the secreted immune cytokines can further boost the recruitment of CD8^+ T cells, which is favorable for the cascade amplification of antitumor immune responses. Next, we evaluated the cytotoxicity of OMP in BMDCs. As shown in Supporting Information Fig. S13, OMP was well tolerated by BMDCs up to a concentration of 90 $\mu\text{g/mL}$ (cell viability >85.0%) with a co-incubation time of 24 h.

3.4. Regulation of PD-L1 by OMP-mediated cuproptosis

Recent studies indicated that intracellular Cu^+ in tumors could affect PD-L1 expression^{36,37}. Therefore, we investigated the effect of OMP-mediated cuproptosis on PD-L1 expression in B16F10 cells. Western blot analysis indicated the decreased total PD-L1 expression in B16F10 cells (Fig. 3A and Fig. S8). As

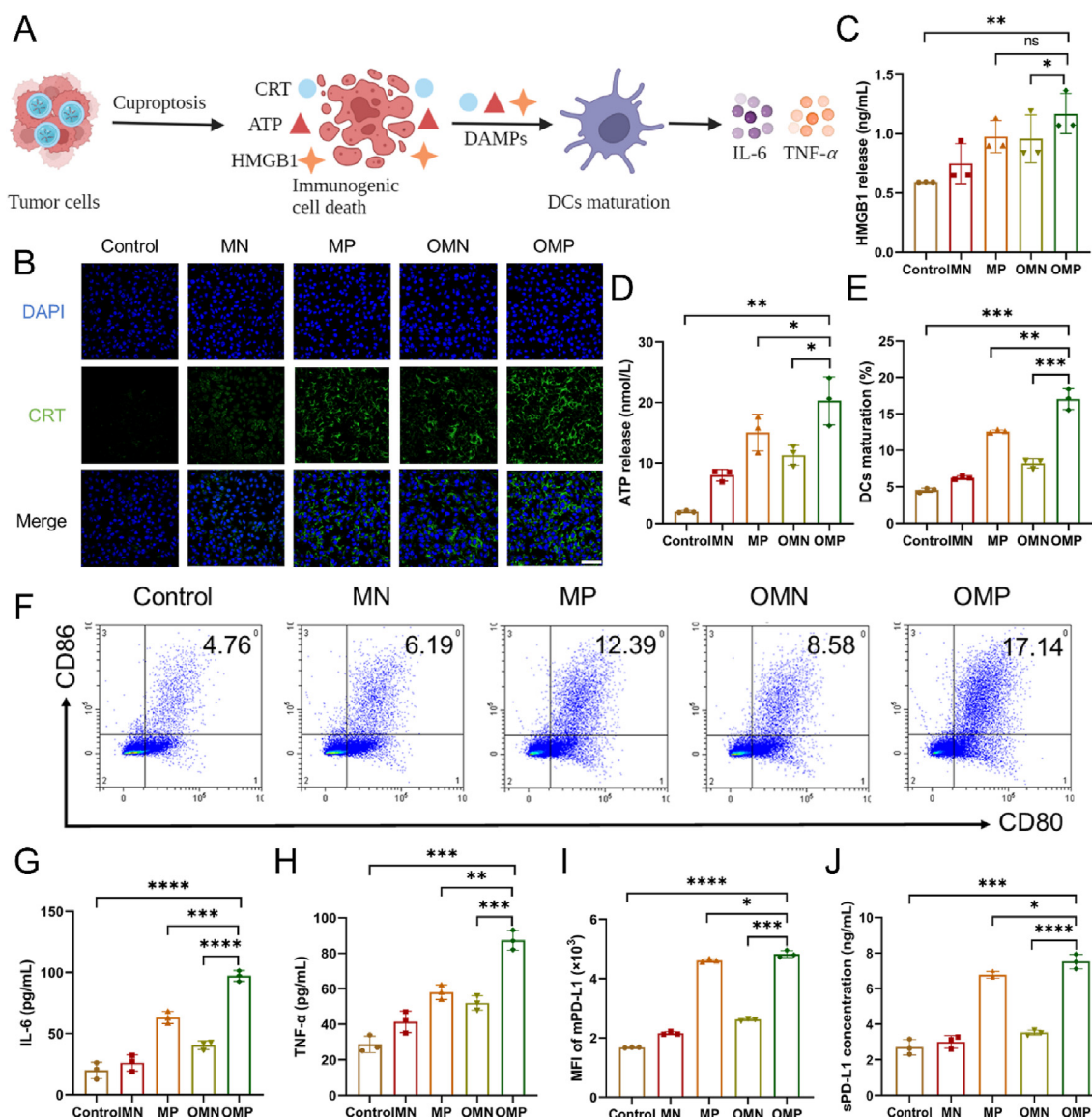


Figure 4 OMP-mediated cuproptosis evoked ICD and regulated PD-L1 in tumor cells. (A) Schematic diagram of the efficacy of OMP-mediated cuproptosis-evoked ICD effect to promote DCs maturation. (B) CRT immunofluorescence images of B16F10 cells in different groups (CRT (AF488, green), Nucleus (DAPI, blue)). Scale bar: 50 μ m. (C) ELISA analysis of HMGB1 release from B16F10 cells after various treatments for 24 h. (D) Extracellular ATP of B16F10 cells in different groups. (E) Corresponding quantitative analysis and (F) representative images of mature DCs (CD11c⁺CD80⁺CD86⁺, gated on CD11c⁺ cells) analyzed by flow cytometry. (G, H) Quantitative analysis of the cytokines secreted by BMDCs in the medium after treatment with different conditions for 24 h, (G) IL-6 and (H) IL-12. (I) Flow cytometry analysis of membrane-associated PD-L1 expression in B16F10 cells after 24-h incubation with different nanoparticles. (J) ELISA analysis of soluble PD-L1 in the supernatant of B16F10 cells after treated with various nanoparticles for 24 h. Data are shown as mean \pm SD ($n = 3$). ns means no significant difference, * $P < 0.05$, ** $P < 0.01$, *** $P < 0.001$, **** $P < 0.0001$.

shown using immunofluorescence, the expression of PD-L1 in the OMP group was lower than those in other groups (Supporting Information Fig. S14A). The qRT-PCR analysis of PD-L1 mRNA expression also indicated significantly reduced expression in B16F10 cells after treatment with OMP for 24 h (Fig. S14B). However, flow cytometry and enzyme-linked immunosorbent assay (ELISA) results showed that the expression of mPD-L1 on B16F10 cells, as well as sPD-L1 secreted into the supernatant, were increased after treatment with OMP for 24 h (Fig. 4I and J). Studies have shown that mPD-L1 in tumor cells and sPD-L1 in peripheral blood could promote CD8⁺ T cells-

mediated cytotoxicity when associated with aPD-L1 and couldn't induce immune tolerance and escape^{38–41}. Based on this observation, the combined administration of OMP and aPD-L1 could be a promising form of cancer immunotherapy.

3.5. Mucosa permeation ability of OMP

The mucosa permeability of OMP was investigated using Caco-2 cells. Caco-2 cells with long culture time (15 days) possess a secreted mucus layer that can evaluate the mucosa penetration capability of OMP (Supporting Information Fig. S15)^{42,43}. First, the

cytotoxicity of MP and OMP were tested against Caco-2 cells. The MP and OMP exhibited cytotoxicity in a dose-dependent manner (Supporting Information Fig. S16). To clarify the effect of OPDEA surface properties on transmucosal capacity at the cellular level, a monolayer composed of Caco-2 cells was used to measure the transepithelial electrical resistance (TEER) and apparent permeability coefficient (Papp) after co-incubation with different nanoparticles. FAM fluorescence dye labeled siPDK was used in this experiment. According to previous studies, zwitterionic carrier platform was able to address mucus barriers, and drastically enhance the transport of drugs payload without opening tight junctions⁴⁴. Consistent with the reports, the TEER values of Caco-2 in OMP group were unchanged during the experiment, suggesting that the cell monolayer was intact and the transport occurred only through the transcellular pathways (Supporting Information Fig. S17A). The transmucosal capacity of each nanoformulation was further tested by measuring the Papp, which is defined as the rate of the nanoparticles crossing the Caco-2 monolayer on a Transwell membrane. As shown in Fig. S17B, siPDK and MP hardly crossed the monolayer, while OMP crossed the monolayer over time. The estimated Papp of OMP was 5.1×10^{-5} cm/s, which was about 5.4- and 2.7-fold of the siPDK and MP at 3 h, respectively. This suggested that the enhanced mucosa permeability was associated with the OPDEA surface properties. Furthermore, the transmucosal capability of different nanoformulations across the Caco-2 monolayer was also recorded by CLSM. The green fluorescence signal originated from the FAM-labeled siPDK, and the most conspicuous transportation signal across the mucus layer occurred in the OMP group (Fig. S17C). These results indicated that OMP with the OPDEA surface exhibited efficient transmucosal capacity.

3.6. *In vivo* transmucosal penetration and lung accumulation ability of OMP

We designed OMP that are intended to be inhaled by mice. To ensure that the atomization process exerted no impact on OMP properties, we collected the formed spray and conducted stability tests. A microsyringe aerosolizer (MSA-250, PennCentury, USA) was utilized for atomization experiments, which could atomize liquid nanoparticles in a high-pressure way to achieve precise quantitative and high-concentration direct pulmonary administration (Supporting Information Fig. S18A). After atomization, the particle size, PDI, and zeta potential of OMP showed negligible changes (Fig. S18B and S18C), indicating the structure integrity of OMP was maintained during the nebulization process. Furthermore, TEM image of OMP after atomization displayed a morphology similar to that of OMP without atomization (Fig. S18D). These findings suggest that OMP could be atomized with high stability, which is important for their use in inhaled therapies.

We further evaluated the *in vivo* transmucosal absorption and lung accumulation behaviors of different formulations by tracking and visualizing the Cy5 signal in female C57BL/6J mice (siPDK labeled with Cy5). At 1, 6, and 24 h after inhalation or intravenous injection of Cy5-MP and Cy5-OMP, mice were sacrificed, and their normal tissues including heart, lungs, liver, spleen, and kidney were collected for *ex vivo* fluorescence imaging, and the lungs collected at 1 h were used for immunofluorescence staining. The *ex vivo* imaging showed bright fluorescence spreading across the whole lung after inhalation administration of Cy5-OMP and retaining for at least 24 h (Fig. 5A). Moreover, the intravenously injected Cy5-OMP was mainly manifested in the liver (accounting

for 70.5%) with little reaching the lungs (4.1%), due to its tendency of being arrested by the reticuloendothelial system. After inhalation, the lungs accumulation of Cy5-OMP significantly increased by approximately 94.3-, 198.3-, and 177.9-fold higher than the intravenous injection of Cy5-OMP at 1, 6, and 24 h, respectively, manifesting a superior drug accumulation and retention in lung lesions (Fig. 5B–D). In addition, the stronger Cy5 fluorescence was observed in the lungs treated with inhalation of Cy5-OMP than inhalation of Cy5-MP at 1, 6, and 24 h, which was 9.3-, 3.7-, and 5.4-fold, respectively (Fig. 5E). These confirmed that OPDEA-based vectors exhibited excellent mucosa penetration and lung retention capability. The distribution of Cy5-labeled nanoparticles in lungs at 1 h was further sliced and imaged by CLSM. As expected, confocal images of the lungs collected from mice treated with inhalation of Cy5-OMP showed stronger Cy5 fluorescence. This suggested OPDEA-coated vectors significantly improved the transmucosal penetration and lung deposition ability. In summary, OMP possessed superb transmucosal penetration and lung accumulation properties. Next, to evaluate *in vivo* pharmacokinetics, the plasma levels of Cy5-siPDK were measured after inhalation or intravenous injection of Cy5-MP and Cy5-OMP. After 24 h of inhalation, the Cy5-siPDK relative content in the blood of the mice in the OMP group was $12.0 \pm 2.5\%$ (Supporting Information Fig. S19). The result demonstrated that Cy5-OMP for inhalation administration had better long-term blood circulation ability. These satisfactory properties of OMP made it an ideal inhalable nanopatform candidate for the treatment of lung metastasis.

3.7. *In vivo* anti-metastatic effects of OMP-mediated cuproptosis combined with aPD-L1

Inspired by the considerable antitumor effects and sufficient immune activation of OMP *in vitro*, we then explored the anti-metastatic efficacy of inhalation of OMP and OMP in combination with PD-L1 checkpoint blockade therapy *in vivo* using the B16F10 melanoma lung metastasis model. As one of the most invasive cancers, melanoma is likely to metastasize to lung tissues through circulatory system. After 7-day tumor inoculation, mice were randomly divided into the following five groups, including 1: PBS (inh), 2: aPD-L1 (i.v.), 3: OMP (i.v.), 4: OMP (inh), and 5: OMP (inh) + aPD-L1 (i.v.) (where inh represents inhalation and i.v. for intravenous injection). As shown in Fig. 6A, OMP (5 mg/kg) was inhaled or injected intravenously for four times every 4 days, and aPD-L1 (3 mg/kg) were applied together after inhalation for 24 h to achieve the best therapeutic efficiency. In the parallel experiment, mice were sacrificed on Day 18 and the number of metastasis foci on the surface of lungs collected in different groups was counted to evaluate the therapeutic efficacy. As shown in Fig. 6B and Supporting Information Fig. S20, compared with OMP (i.v.), mice treated with OMP (inh) exhibited a significant reduction in the numbers of lesions on the lung surface, especially when combined with aPD-L1, which indicated that the combination of OMP and aPD-L1 could effectively inhibit the lung metastasis. In addition, hematoxylin and eosin (H&E) staining of the lung tissues also demonstrated the excellent anti-metastatic efficiency of OMP (inh) combination with aPD-L1 (i.v.) (Fig. 6G). Moreover, the comparison between OMP (i.v.) and OMP (inh) groups showed significant differences. The above results demonstrated that inhalation of OMP had a better therapeutic effect on lung metastasis than that of intravenous injection due to the stronger targeting accumulation and retention capacity of OMP toward the lung.

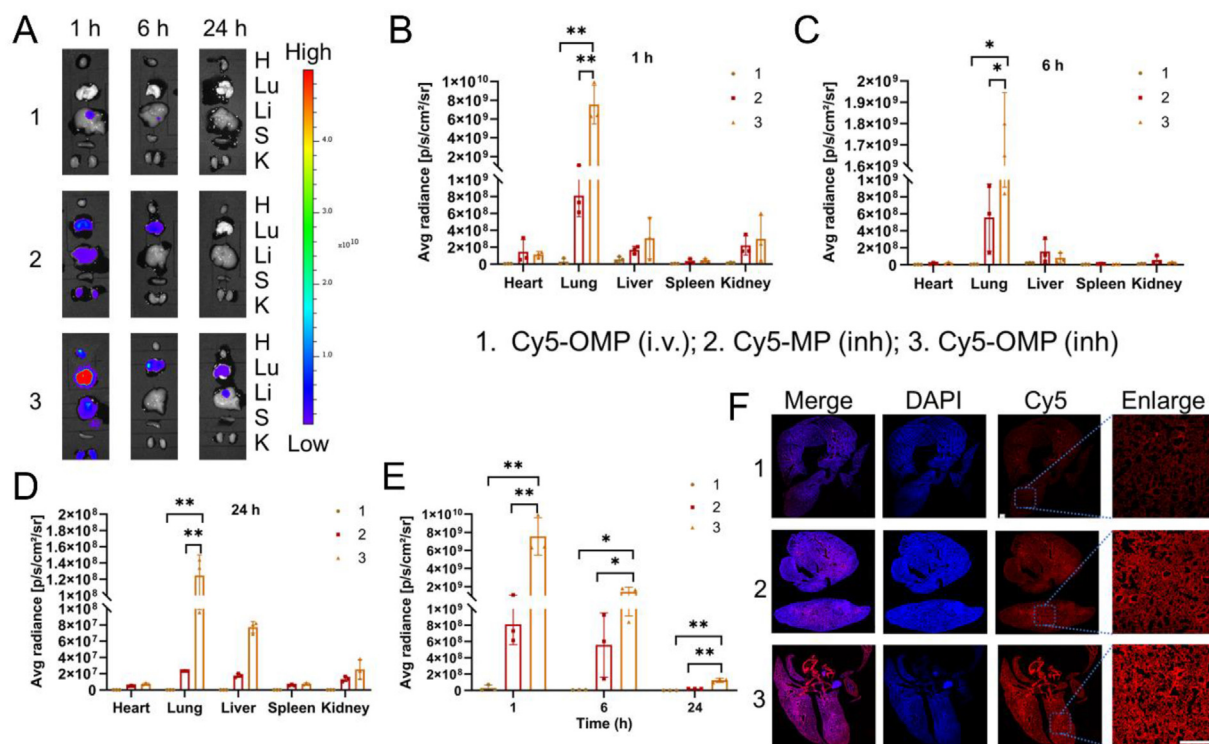


Figure 5 Mucosa penetration and lung retention of OMP *in vivo*. (A) *Ex vivo* fluorescence imaging of heart, lungs, liver, spleen, and kidney following intravenous injection or inhalation of Cy5-MP and Cy5-OMP at timed intervals (H, heart; Lu, lung; Li, liver; S, spleen; K, kidney). siPDK was labeled with Cy5 to display the biodistribution of the drug. (B–D) Quantification fluorescence analysis of heart, lungs, liver, spleen, and kidney at (B) 1 h, (C) 6 h, and (D) 24 h. (E) Quantification fluorescence analysis of lungs at 1, 6, and 24 h after timed intervals of intravenous injection or inhalation of Cy5-MP and Cy5-OMP. (F) CLSM of lung sections at 1 h after intravenous injection or inhalation of Cy5-MP and Cy5-OMP. The red fluorescence was from Cy5. The section highlighted in the left pics was zoomed in the right images. The scale bars correspond to 1 mm. The groups are as follows: 1, Cy5-OMP (i.v.); 2, Cy5-MP (inh); 3, Cy5-OMP (inh); (where inh represents inhalation and i.v. for intravenous injection). Data are shown as mean \pm SD ($n = 3$). * $P < 0.05$, ** $P < 0.01$.

Furthermore, we assessed the influence of different treatments on mice survival. As shown in Fig. 6C, OMP (inh) + aPD-L1 (i.v.) administration significantly prolonged the survival. Simultaneously, the body weight was monitored every two days until Day 18. As shown in Fig. 6D, the stable body weight curve showed that there was no systematic toxicity after diverse treatments.

Encouraged by the superior therapeutic effect achieved by the OMP (inh) + aPD-L1 (i.v.) treatment, the anti-metastatic mechanism was further explored *in vivo*. Subsequently, PDK1 mRNA qRT-PCR analysis, lactate production, cuproptosis-related proteins expression, and DLAT immunohistochemistry staining in lung tissues were carried out. Lung metastasis treated with OMP (inh) and OMP (inh) + aPD-L1 (i.v.) groups exhibited lower PDK1 expression compared to PBS, aPD-L1 (i.v.), and OMP (i.v.) groups (Fig. 6E). Moreover, the lactate contents were significantly decreased in OMP (inh)- and OMP (inh) + aPD-L1 (i.v.)-treated lung tissues. These results revealed that inhalation of OMP could effectively suppress intratumoral glycolysis, which might be beneficial to cuproptosis induction. As shown in Supporting Information Fig. S21, the levels of ACO-2, Lip-DLAT, DLAT, and FDX1 in OMP (inh) and OMP (inh) + aPD-L1 (i.v.) were significantly decreased compared with control group, verifying the effective activation of cuproptosis *in vivo*. Moreover, the most pronounced aggregation of DLAT was observed in OMP (inh) + aPD-L1 (i.v.) group (Fig. 6G), verifying the most powerful ability to induce cuproptosis *in vivo*. Taken together, these results

indicated the multifaceted effects provided by OMP (inh) + aPD-L1 (i.v.) group could significantly induce tumor cells cuproptosis and further effectively suppress lung metastasis.

3.8. Anti-metastatic immunity evoked by combining OMP-mediated cuproptosis with aPD-L1

In consideration of the above comprehensive results, we further investigated the underlying mechanism of OMP-mediated immunotherapy. The exposure of CRT at lung tissues was detected *via* immunofluorescence staining (Fig. 7A). Compared with the OMP (i.v.) group, OMP (inh) and OMP (inh) + aPD-L1 (i.v.) groups could induce the exposure CRT to a certain extent, indicating that ICD effect was evoked by inhaling OMP. In addition, the maturation of DCs ($CD45^+CD11c^+CD80^+CD86^+$) in tumor-draining lymph nodes was detected by flow cytometry (Fig. 7B, Figs. S22A and S23A). The percentage of DCs maturation in OMP (inh) + aPD-L1 (i.v.) group was significantly elevated to 1.8%, which was approximately 2.5- and 1.7-fold relative to PBS and aPD-L1 groups, respectively, revealing the satisfactory effect on the enhancement of DCs maturation.

Tumor immunotherapy requires biomarkers and sPD-L1 in plasma has been considered a predictor for response to immunotherapy in the clinic^{38,45}. We thus evaluated the ability of OMP combination with aPD-L1 to modulate the PD-L1 expression and sPD-L1 secretion of B16F10 melanoma lung

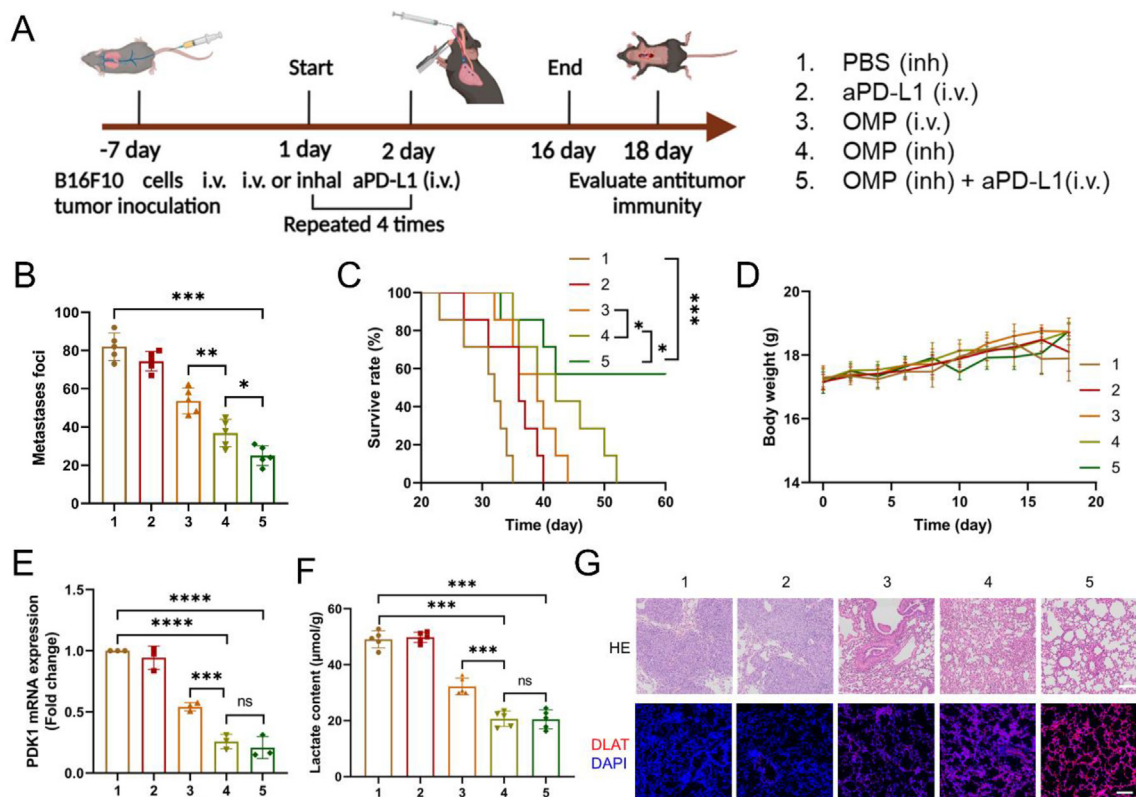


Figure 6 Evaluation of anti-metastatic effect of inhalable OMP combined with aPD-L1 in B16F10 melanoma lung metastasis model. (A) Schematic illustration showing the design of animal experiments. (B) Numbers of metastatic foci on the surface of lungs after different treatments ($n = 5$). (C) Survival curves of mice with various treatments ($n = 7$). (D) The body weight of mice was recorded for various treatments ($n = 5$). (E) qRT-PCR analysis of the PDK1 mRNA expression in lung metastasis after treatment with various conditions ($n = 3$). (F) Lactate contents in lung tissues after various treatments ($n = 5$). (G) H&E and DLAT staining images of lungs after various treatments. DLAT was labeled with Alexa Fluor 555 (red) and cell nuclei were labeled with DAPI (blue). Scale bar: 100 μm . Data are shown as mean \pm SD. ns means no significant difference, * $P < 0.05$, ** $P < 0.01$, *** $P < 0.001$, **** $P < 0.0001$.

metastasis. As indicated in Fig. 7C, OMP (inh) and OMP (inh) + aPD-L1 (i.v.) led to a significant decrease of PD-L1 expression compared to PBS-treated mice, suggesting the capacity of OMP to down-regulate PD-L1 expression. Analysis of sPD-L1 in plasma using ELISA showed that sPD-L1 levels were higher in OMP-treated mice than those in the PBS group. In contrast, combination treatment with OMP and aPD-L1 significantly decreased sPD-L1 levels in the circulation (Fig. 7D). These results indicated that OMP-induced secretion of sPD-L1 reduced the activity of CD8^+ T cells, and combination with aPD-L1 reenergized exhausted T cells to promote tumor suppression.

Tumor progression is intimately related to the overall state of the immune system. In most instances, TME is in an immunosuppressive state, manifested as the exhaustion of CD8^+ T cells, abundant M2-polarized macrophages, and increased MDSCs and Tregs development⁴⁶. The superior *in vivo* anti-metastatic efficacy of the combination of inhalation OMP and aPD-L1 immunotherapy could be attributed to the successful activation of chain-like immune responses. To evaluate the mechanisms underlying the response of immune cells and the expression of major immune cell cytokines in lung tissues were evaluated using a subset of the tested mice on Day 18. We first quantified tumor-infiltrating cytotoxic CD8^+ T cells using flow cytometry. Under the synergistic activity of OMP and PD-L1 checkpoint

blockade, the proportion of CD8^+ T cells ($\text{CD45}^+\text{CD3}^+\text{CD8}^+$) in the OMP (inh) + aPD-L1 (i.v.) group was significantly greater than in the PBS and aPD-L1 (i.v.) groups (Fig. 7E, Figs. S22B and S23B), exhibiting 1.6- and 1.4-fold increases, respectively, indicating OMP combination with aPD-L1 possessed the powerful ability of facilitating CD8^+ T cells infiltration. In addition, M1-type macrophages ($\text{CD45}^+\text{F4/80}^+\text{CD86}^+\text{CD206}^-$) and M2-type macrophages ($\text{CD45}^+\text{F4/80}^+\text{CD86}^+\text{CD206}^+$) at the lung tissues were also quantified *via* flow cytometry. Compared to the PBS group, the OMP (inh) and aPD-L1 (i.v.) combination led to a remarkable increase of tumor-infiltrating M1-type macrophages and significant reduction of M2-type macrophages, ultimately producing a 3.3-fold enhancement of the M1/M2 ratio (Fig. 7F–H, Figs. S22C and S23C). The immunosuppressive MDSCs and Tregs severely suppress anti-metastatic immune responses in cancer immunotherapy^{47,48}. Therefore, we further explored the capacity of the OMP (inh) + aPD-L1 (i.v.) to relieve *in vivo* immunosuppression of lung metastasis using flow cytometry. As shown in Fig. 7I, Figs. S22D and S23D, the fraction of immunosuppressive Tregs ($\text{CD45}^+\text{CD4}^+\text{Foxp3}^+$) exhibited a sharp decrease upon treatment with the OMP (inh) + aPD-L1 (i.v.), being more effective in down-regulating Tregs as compared to aPD-L1 and OMP alone. In addition, lung metastasis had a high percentage of MDSCs ($\text{CD45}^+\text{CD11b}^+\text{Gr-1}^+$), and aPD-L1 treatment only led to a

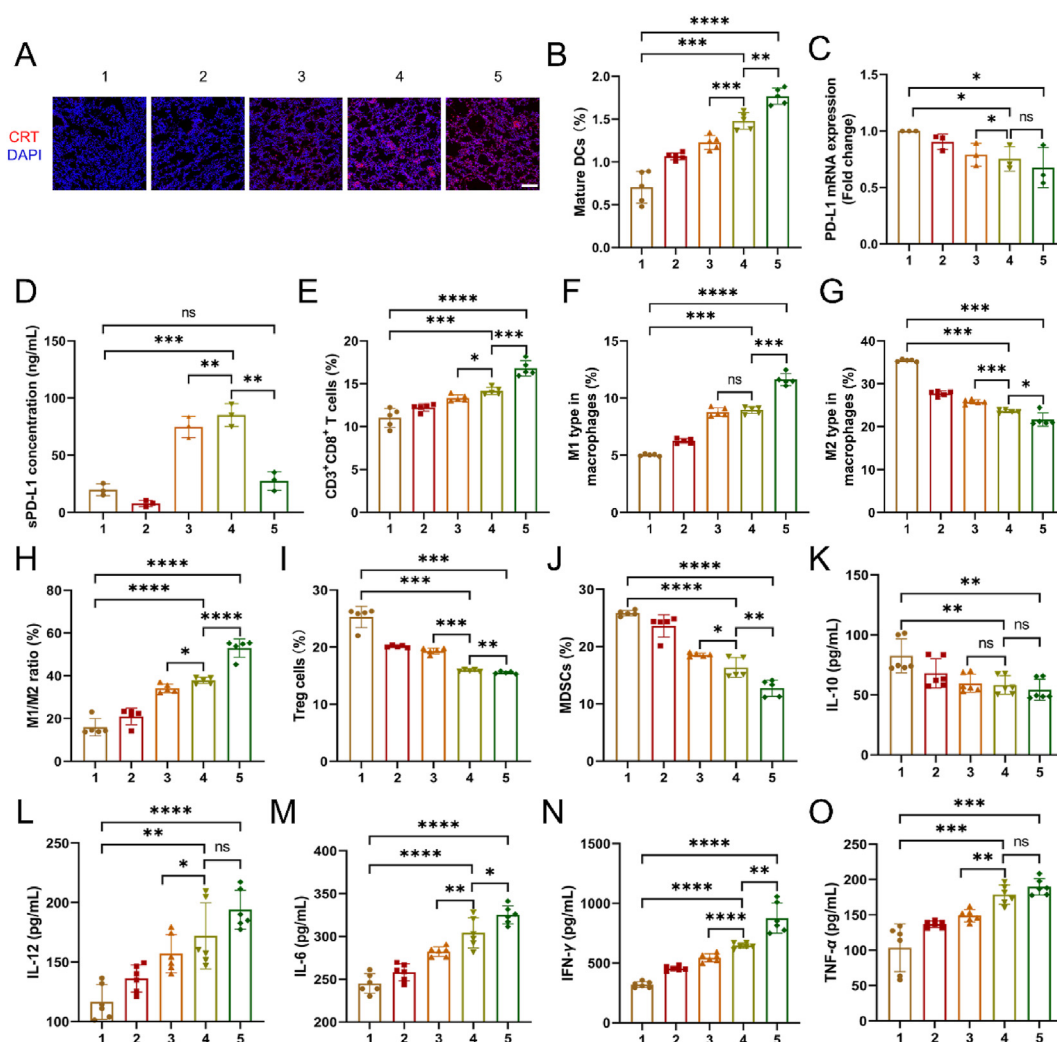


Figure 7 *In vivo* immune activation and exertion of potent antimetastatic efficacy with combined inhalable OMP and aPD-L1. (A) Immunofluorescence images of CRT in lung sections ($n = 3$). CRT was labeled with Alexa Fluor 555 (red) and cell nuclei were labeled with DAPI (blue). Scale bars: 100 μm . (B) The semiquantitative analysis from flow cytometry of DCs in tumor-draining lymph nodes ($n = 5$). (C) qRT-PCR analysis of the PD-L1 expression in lung metastasis sites after various treatments ($n = 3$). (D) Soluble PD-L1 secretion in the blood serum of each group ($n = 3$). (E) Flow cytometric analysis of CD8⁺ T cells in lung tissues after different treatments ($n = 5$). (F–H) The frequency of (F) M1-type macrophages, (G) M2-type macrophages, and (H) M1/M2 ratio in metastatic lungs from each treatment ($n = 5$). (I and J) Flow cytometric analysis of (I) Tregs and (J) MDSCs in lung samples extracted from mice given treatments ($n = 5$). (K–O) Concentrations of (K) IL-10, (L) IL-12, (M) IL-6, (N) IFN- γ , and (O) TNF- α secreted in lung tissues evaluated by ELISA ($n = 6$). 1: PBS (inh), 2: aPD-L1 (i.v.), 3: OMP (i.v.), 4: OMP (inh), and 5: OMP (inh) + aPD-L1 (i.v.). Data are shown as mean \pm SD. ns means no significant difference, * $P < 0.05$, ** $P < 0.01$, *** $P < 0.001$, **** $P < 0.0001$.

minimal decrease of MDSCs proportion. In contrast, the OMP (inh)+aPD-L1 (i.v.) group resulted in a distinct decrease of MDSCs fraction (Fig. 7J, Figs. S22E and S23E), affirming the effectiveness of this combination to relieve immunosuppression microenvironment of lung metastasis. Furthermore, the concentrations of different cytokines secreted in the lung tissues were evaluated by ELISA. As we expected, the IL-10 concentrations, which induced the polarization of M2 macrophages, greatly decreased in the lungs treated with the OMP (inh) + aPD-L1 (i.v.) group (Fig. 7K). The concentrations of IL-12 and IL-6, which play important roles in activating CD8⁺ T cells, significantly increased with the treatment of OMP (inh) + aPD-L1 (i.v.) (Fig. 7L and M). Cytokines including IFN- γ and TNF- α were also obviously increased, which further indicated the stronger cellular immune responses induced by OMP and aPD-

L1 combination (Fig. 7N and O). Collectively, the results confirmed that OMP and aPD-L1 combination could reverse the immunosuppressive TME and trigger an effective anti-metastatic immune response. Hence, cooperative cuproptosis and immune checkpoint blockade can effectively activate immune responses *via* recruiting tumor-attacking immune cells and dismantling *in vivo* immunosuppression.

3.9. *In vivo* biosafety and metabolism analysis of inhalable OMP

The potential *in vivo* toxicity is always a considerable concern for nanomaterials used in biomedicine. To evaluate the safety of inhalable OMP nanoparticles, healthy female C57BL/6J mice were inhaled PBS and OMP (at a total dose of 5 mg/kg) for four

times every 4 days. Thereafter, the major organs of mice were collected for H&E analysis on Day 18. As shown in [Supporting Information Fig. S24A](#), we could not observe significant alveolar collapse, injury of alveolar epithelial cells, and inflammatory cell infiltration, suggesting that there were negligible lung toxicity and inflammation caused by inhalation administrations of OMP. Moreover, the H&E staining images also indicated that inhalation of OMP would not impact the other main organs (heart, liver, spleen, and kidney). The above results demonstrated that inhalation of OMP didn't cause histological damage to lung tissues and other organs, suggesting their preferable *in vivo* safety. Furthermore, the hemocompatibility of OMP nanoparticles was performed. No hemolysis was observed for OMP nanoparticles up to a concentration of 400 µg/mL ([Fig. S24B](#)), indicating the high biocompatibility of the nanocomposite. We further conducted blood chemistry tests including liver functions [aspartate aminotransferase (AST) and alanine aminotransferase (ALT)] and renal function markers [creatinine (CRE) and blood urea nitrogen (BUN)] on blood serum ([Fig. S24C–S24F](#)). The results revealed that the levels of all blood biochemical parameters fell within the normal range, indicative of the stable order in both liver and kidney. All of the above results indicated a good biocompatibility of this OMP system.

We further explored the retention time in lungs and clearance pathway of OMP after inhalation administration. On the basis of the Cu contents measured by ICP-MS, a retention time in lungs after inhalation of OMP was carried out. After inhalation of OMP, the Cu contents of OMP in lungs were found to be 45.3%, which proved that OMP mainly accumulated in lungs. Moreover, the levels of Cu significantly decreased over time. After 5 days, the amounts of Cu showed a drastic decrease to be <3.0% ID/g in lungs, suggesting that the majority of OMP was cleared out from the mice body ([Supporting Information Fig. S25A](#)). In addition, we investigated the clearance pathway of OMP after inhalation administration. ICP-MS was used to analyze the metabolites in mice, including urine and feces. After inhaling OMP for 3 days, most of the Cu could be detected in the urine and feces of the mice. Time-dependent analysis of the Cu content revealed that most of the inhaled OMP could be found in the urine within 9 days, demonstrating that OMP could be gradually eliminated through the renal route, and the remaining part could be metabolized slowly *via* the feces ([Fig. S25B](#)). These results overall point out that OMP is highly effective and biosafe.

4. Conclusions

In summary, we developed a copper-based nanoplatform (termed OMP) for sensitizing cancer cells to cuproptosis and activating cuproptosis-mediated immunotherapy of lung metastasis by inhalation administration. OMP with OPDEA clocks could overcome the pulmonary mucosal barriers and greatly enhance the intratumoral accumulation by inhalation administration. Within tumor cells, OMP not only released Cu⁺ under acidic and GSH conditions, but also effectively inhibited intracellular glycolysis and ATP production, which down-regulated Cu⁺ efflux protein ATP7B expression and further increased intracellular Cu⁺ accumulation, finally inducing cancer cells cuproptosis. In addition, OMP-mediated cuproptosis acted as the ICD evoker to enhance the tumor cell related immunogenicity and promote immune activation (DCs maturation and CD8⁺ T cells infiltration). More importantly, OMP-induced cuproptosis up-regulated membrane-associated PD-L1 expression and induced soluble PD-L1 secretion

in B16F10 cells. In lung melanoma metastasis model, OMP could convert the immunosuppressive TME to an immune-activating environment, thereby inhibiting the growth of metastatic lung tumors without obvious side effects. Furthermore, OMP-induced cuproptosis collaborated with PD-L1 checkpoint blockade could provoke more powerful anti-tumor immunity. Consequently, OMP represents the effective inhalable system to perform the synergistic therapeutic strategy *via* inducing cuproptosis and combining with PD-L1 checkpoint blockade that prove to be a powerful tool against lung metastasis.

Acknowledgments

This work was partially funded by the Key R&D Programs of Shandong Province, China (Grant Nos. 2018CXGC1411 and 2021CXGC010514).

Author contributions

Zhongxi Zhao and Chongzheng Yan conceived and administered the project. Chongzheng Yan, Ying Liu, Guozhi Zhao, Huatian Yang, Huaiyou Lv, Genju Li, Yuhan Li, Yaqing Fu, Fengqin Sun, Yafei Feng, and Yizhe Li conducted the investigation. Chongzheng Yan performed experiments. Zhongxi Zhao applied for the funding. Chongzheng Yan wrote the manuscript. Zhongxi Zhao supervised the project. All of the authors have read and approved the final manuscript.

Conflicts of interest

The authors declare no conflicts of interest.

Appendix A. Supporting information

Supporting data to this article can be found online at <https://doi.org/10.1016/j.apsb.2024.01.017>.

References

- Mithoowani H, Febbraro M. Non-small-cell lung cancer in 2022: a review for general practitioners in oncology. *Curr Oncol* 2022;**29**: 1828–39.
- He G, Nie JJ, Liu X, Ding Z, Luo P, Liu Y, et al. Zinc oxide nanoparticles inhibit osteosarcoma metastasis by downregulating beta-catenin *via* HIF-1 α /BNIP3/LC3B-mediated mitophagy pathway. *Bioact Mater* 2022;**19**:690–702.
- Eisenstein M. New lung-cancer drugs extend survival times. *Nature* 2020;**587**:S10–2.
- Wang M, Herbst RS, Boshoff C. Toward personalized treatment approaches for non-small-cell lung cancer. *Nat Med* 2021;**27**:1345–56.
- Chang A. Chemotherapy, chemoresistance and the changing treatment landscape for NSCLC. *Lung Cancer* 2011;**71**:3–10.
- Puglisi M, Dolly S, Faria A, Myerson JS, Popat S, O'Brien MER. Treatment options for small cell lung cancer—do we have more choice?. *Br J Cancer* 2010;**102**:629–38.
- Shen JJ, Lin MH, Ding MB, Yu NY, Yang C, Kong DP, et al. Tumor immunosuppressive microenvironment modulating hydrogels for second near-infrared photothermal-immunotherapy of cancer. *Mater Today Bio* 2022;**16**:100416.
- Xu YY, Xiong JY, Sun XY, Gao HL. Targeted nanomedicines remodeling immunosuppressive tumor microenvironment for enhanced cancer immunotherapy. *Acta Pharm Sin B* 2022;**12**:4327–47.
- Ma SC, Tang XR, Long LL, Bai X, Zhou JG, Duan ZJ, et al. Integrative evaluation of primary and metastatic lesion spectrum to guide

- anti-PD-L1 therapy of non-small cell lung cancer: results from two randomized studies. *Oncimmunology* 2021;**10**:1909296.
10. Tsvetkov P, Coy S, Petrova B, Dreishpoon M, Verma A, Abdusamad M, et al. Copper induces cell death by targeting lipoylated TCA cycle proteins. *Science* 2022;**375**:1254–61.
 11. Ning SP, Lyu M, Zhu DM, Lam JWY, Huang QQ, Zhang TF, et al. Type-I AIE photosensitizer loaded biomimetic system boosting cuproptosis to inhibit breast cancer metastasis and rechallenge. *ACS Nano* 2023;**17**:10206–17.
 12. Golias T, Kery M, Radenkovic S, Papandreou I. Microenvironmental control of glucose metabolism in tumors by regulation of pyruvate dehydrogenase. *Int J Cancer* 2019;**144**:674–86.
 13. Peng F, Wang JH, Fan WJ, Meng YT, Li MM, Li TT, et al. Glycolysis gatekeeper PDK1 reprograms breast cancer stem cells under hypoxia. *Oncogene* 2018;**37**:1062–74.
 14. Saunier E, Benelli C, Bortoli S. The pyruvate dehydrogenase complex in cancer: an old metabolic gatekeeper regulated by new pathways and pharmacological agents. *Int J Cancer* 2016;**138**:809–17.
 15. Anwar S, Shamsi A, Mohammad T, Islam A, Hassan MI. Targeting pyruvate dehydrogenase kinase signaling in the development of effective cancer therapy. *Biochim Biophys Acta Rev Cancer* 2021;**1876**:188568.
 16. Bedingfield SK, Colazo JM, Yu F, Liu DD, Jackson MA, Himmel LE, et al. Amelioration of post-traumatic osteoarthritis via nanoparticle depots delivering small interfering RNA to damaged cartilage. *Nat Biomed Eng* 2021;**5**:1069–83.
 17. Zhao ZY, Dong SM, Liu Y, Wang JX, Ba L, Zhang C, et al. Tumor microenvironment-activable manganese-boosted catalytic immunotherapy combined with PD-1 checkpoint blockade. *ACS Nano* 2022;**16**:20400–18.
 18. Wang YX, Ding YW, Yao D, Dong H, Ji CW, Wu JH, et al. Copper-based nanoscale coordination polymers augmented tumor radioimmunotherapy for immunogenic cell death induction and T-cell infiltration. *Small* 2021;**17**:e2006231.
 19. Zhang JL, Sun XY, Zhao XF, Yang CR, Shi MH, Zhang BZ, et al. Combining immune checkpoint blockade with ATP-based immunogenic cell death amplifier for cancer chemo-immunotherapy. *Acta Pharm Sin B* 2022;**12**:3694–709.
 20. Li ZL, Lai XQ, Fu SQ, Ren L, Cai H, Zhang H, et al. Immunogenic cell death activates the tumor immune microenvironment to boost the immunotherapy efficiency. *Adv Sci (Weinh)* 2022;**9**:e2201734.
 21. Zhang XG, Tang JJ, Li C, Lu Y, Cheng LL, Liu J. A targeting black phosphorus nanoparticle based immune cells nano-regulator for photodynamic/photothermal and photo-immunotherapy. *Bioact Mater* 2020;**6**:472–89.
 22. He YP, Li DF, Wu L, Yin XZ, Zhang XJ, Patterson LH, et al. Metal-organic frameworks for gene therapy and detection. *Adv Funct Mater* 2023;**33**:16.
 23. Guo LN, Zhong SH, Liu P, Guo M, Ding JS, Zhou WH. Radicals scavenging MOFs enabling targeting delivery of siRNA for rheumatoid arthritis therapy. *Small* 2022;**18**:e2202604.
 24. Kumar M, Jha A, Dr M, Mishra B. Targeted drug nanocrystals for pulmonary delivery: a potential strategy for lung cancer therapy. *Expert Opin Drug Deliv* 2020;**17**:1459–72.
 25. Jin QT, Zhu WJ, Zhu JF, Zhu JJ, Shen JJ, Liu Z, et al. Nanoparticle-mediated delivery of inhaled immunotherapeutics for treating lung metastasis. *Adv Mater* 2021;**33**:e2007557.
 26. Perry JL, Tian SM, Sengottuvel N, Harrison EB, Gorentla BK, Kapadia CH, et al. Pulmonary delivery of nanoparticle-bound toll-like receptor 9 agonist for the treatment of metastatic lung cancer. *ACS Nano* 2020;**14**:7200–15.
 27. Zhang TT, Chen YM, Ge YY, Hu YZ, Li M, Jin YG. Inhalation treatment of primary lung cancer using liposomal curcumin dry powder inhalers. *Acta Pharm Sin B* 2018;**8**:440–8.
 28. Fu FQ, Wang WH, Wu LJ, Wang WH, Huang ZW, Huang Y, et al. Inhalable biomimetic liposomes for cyclic Ca²⁺-burst-centered endoplasmic reticulum stress enhanced lung cancer ferroptosis therapy. *ACS Nano* 2023;**17**:5486–502.
 29. Ma ZW, Wang HM, Shi ZF, Yan FY, Li QT, Chen JJ, et al. Inhalable GSH-triggered nanoparticles to treat commensal bacterial infection *in situ* lung tumors. *ACS Nano* 2023;**17**:5740–56.
 30. Fan WF, Wei QY, Xiang JJ, Tang YS, Zhou Q, Geng Y, et al. Mucus penetrating and cell-binding polyzwitterionic micelles as potent oral nanomedicine for cancer drug delivery. *Adv Mater* 2022;**34**:e2109189.
 31. Wang Z, Niu JS, Zhao CQ, Wang XH, Ren JS, Qu XG. A bimetallic metal-organic framework encapsulated with DNzyme for intracellular drug synthesis and self-sufficient gene therapy. *Angew Chem Int Ed Engl* 2021;**60**:12431–7.
 32. Yu B, Wang W, Sun WB, Jiang CH, Lu LH. Defect engineering enables synergistic action of enzyme-mimicking active centers for high-efficiency tumor therapy. *J Am Chem Soc* 2021;**143**:8855–65.
 33. Chen KR, Zhou AW, Zhou XY, Liu YH, Xu YR, Ning XH. An intelligent cell-derived nanorobot bridges synergistic crosstalk between sonodynamic therapy and cuproptosis to promote cancer treatment. *Nano Lett* 2023;**23**:3038–47.
 34. Chen HY, Song HL, Luo YF, Li CF, Wang Y, Liu J, et al. Transcytosis mediated deep tumor penetration for enhanced chemotherapy and immune activation of pancreatic cancer. *Adv Funct Mater* 2023;**33**:e2214937.
 35. Chen SQ, Zhong Y, Fan WF, Xiang JJ, Wang GW, Zhou Q, et al. Enhanced tumour penetration and prolonged circulation in blood of polyzwitterion-drug conjugates with cell-membrane affinity. *Nat Biomed Eng* 2021;**5**:1019–37.
 36. Wu ML, Huang QR, Xie Y, Wu XY, Ma HB, Zhang YW, et al. Improvement of the anticancer efficacy of PD-1/PD-L1 blockade via combination therapy and PD-L1 regulation. *J Hematol Oncol* 2022;**15**:24.
 37. Gong NQ, Zhang YX, Teng XC, Wang YC, Huo SD, Qing GC, et al. Proton-driven transformable nanovaccine for cancer immunotherapy. *Nat Nanotechnol* 2020;**15**:1053–64.
 38. Daassi D, Mahoney KM, Freeman GJ. The importance of exosomal PD-L1 in tumour immune evasion. *Nat Rev Immunol* 2020;**20**:209–15.
 39. Cavazzoni A, Digiacomo G, Alfieri R, La Monica S, Fumarola C, Galetti M, et al. Pemetrexed enhances membrane PD-L1 expression and potentiates T cell-mediated cytotoxicity by anti-PD-L1 antibody therapy in non-small-cell lung cancer. *Cancers (Basel)* 2020;**12**:666.
 40. Jin JK, Yuan PC, Yu W, Lin JT, Xu AK, Xu XD, et al. Mitochondria-targeting polymer micelle of dichloroacetate induced pyroptosis to enhance osteosarcoma immunotherapy. *ACS Nano* 2022;**16**:10327–40.
 41. Guo BD, Yang FY, Zhang LP, Zhao QX, Wang WK, Yin L, et al. Cuproptosis induced by ROS responsive nanoparticles with elesclomol and copper combined with aPD-L1 for enhanced cancer immunotherapy. *Adv Mater* 2023;**35**:e2212267.
 42. Liu DD, Qiao S, Cheng BC, Li DY, Chen JS, Wu QY, et al. Enhanced oral delivery of curcumin via vitamin E TPGS modified nanodiamonds: a comparative study on the efficacy of non-covalent and covalent conjugated strategies. *AAPS PharmSciTech* 2020;**21**:187.
 43. Zhou YH, Chen ZX, Zhao D, Li D, He CL, Chen XS. A pH-triggered self-unpacking capsule containing zwitterionic hydrogel-coated MOF nanoparticles for efficient oral exendin-4 delivery. *Adv Mater* 2021;**33**:e2102044.
 44. Han XF, Lu Y, Xie JB, Zhang ES, Zhu H, Du H, et al. Zwitterionic micelles efficiently deliver oral insulin without opening tight junctions. *Nat Nanotechnol* 2020;**15**:605–14.
 45. Cordonnier M, Nardin C, Chanteloup G, Derangere V, Algros MP, Arnould L, et al. Tracking the evolution of circulating exosomal-PD-L1 to monitor melanoma patients. *J Extracell Vesicles* 2020;**9**:1710899.
 46. Neophytou CM, Panagi M, Stylianopoulos T, Papageorgis P. The role of tumor microenvironment in cancer metastasis: molecular mechanisms and therapeutic opportunities. *Cancers (Basel)* 2021;**13**:2053.
 47. Tian XY, Shen H, Li ZY, Wang TT, Wang SJ. Tumor-derived exosomes, myeloid-derived suppressor cells, and tumor microenvironment. *J Hematol Oncol* 2019;**12**:84.
 48. Wang HP, Franco F, Ho PC. Metabolic regulation of Tregs in cancer: opportunities for immunotherapy. *Trends Cancer* 2017;**3**:583–92.